Ocean Modelling 102 (2016) 27–44

Contents lists available at ScienceDirect

Ocean Modelling

journal homepage: www.elsevier.com/locate/ocemod

Performance assessment for an operational ocean model of the Taiwan Strait

Xinyou Lin[a,c], Xiao-Hai Yan[b,c], Yuwu Jiang[a,*], Zhenchang Zhang[d]

[a] State Key Laboratory of Marine Environmental Science, Xiamen University, Xiamen 361005, Fujian, P. R. China
[b] College of Earth, Ocean and Environment, University of Delaware, Newark, Delaware 19716, USA
[c] Joint Institute for Coastal Research and Management (UD/XMU Joint-CRM), Xiamen University, Xiamen 361005, Fujian, P. R. China
[d] College of Computer and Information Science, Fujian Agriculture and Forestry University, Fuzhou, 350002, P. R. China

ARTICLE INFO

Article history:
Received 16 June 2015
Revised 13 April 2016
Accepted 16 April 2016
Available online 19 April 2016

Keywords:
Numerical model
Taiwan Strait
TFOR
Skill assessment

ABSTRACT

The Taiwan Strait Nowcast/Forecast System (TFOR), which is based on the Regional Ocean Modeling System, may be the first operational ocean model to include both tide and circulation processes in the Taiwan Strait. In this study, we assessed the performance of TFOR by investigating the differences between observational data and the results obtained by TFOR, thereby illustrating the ability of TFOR to reproduce significant physical processes. We also evaluated the utility and reliability of TFOR products for successful applications in maritime search and rescue. The mean bias, root mean-squared difference, correlation coefficient (CC), and Willmott skill for the differences in temperature between the cruise observations and the TFOR results were −0.01°C, 1.2°C, 0.87, and 0.92, respectively, and those for the corresponding salinity results were 0.06 PSU, 0.4 PSU, 0.74, and 0.83, respectively. The distributions of the TFOR M_2 harmonic constants indicated that TFOR simulates the tidal characteristics well in the Taiwan Strait. The CC between the Taiwan Strait volume transport based on the TFOR results and the along-strait wind stress was 0.77, thereby indicating that monsoon winds exert an important influence on the variability in volume transport through the Taiwan Strait. Statistical analyses of the TFOR results showed that the annual, spring, summer, autumn, and winter mean transport volumes were 1.16, 1.28, 2.52, 0.80, and 0.04 Sv, respectively. In conclusion, the TFOR is robust and it can simulate the temperature, salinity, and velocity in a reasonable and stable manner.

1. Introduction

The Taiwan Strait (TWS) is located between Taiwan Island and mainland China, where it connects the East China Sea (ECS) to the South China Sea (SCS), as shown in Fig. 1a. Its bottom topography is somewhat complex, but the average water depth is only approximately 60 m. Its major topographic features are presented in Fig. 1a, including the Kuan-Yin Depression (KYD), Changyun Ridge (CYR), Taiwan Bank (TWB), Wuchou Trough (WCT), and Penghu Channel (PHC). The TWS is under a subtropical monsoon regime, where it is dominated by stronger northeasterly winds in the winter and weaker southwesterly winds in the summer (Ke and Hu, 1991). The regional flows in the TWS have been studied for decades based on *in-situ* observations, remote sensing, and numerical modeling (Hu et al., 2010b). The monsoon system has been regarded as the primary force responsible for flow variations in the TWS (Wyrtki, 1961), while it strongly affects the Zhemin Coastal Current (ZCC, marked in Fig. 1a), which flows southwestward in the upper layer along the east coast of mainland China (Hong et al., 2011a). The SCS Warm Current near the TWB flows northeastward all year round together with the Kuroshio Branch Current (KBC, marked in Fig. 1), and it is considered another cause of flow variations in the TWS (Guan and Chen, 1964; Guan, 1978a, 1978b). Nitani (1972) described the surface coastal current flows in the TWS, including a southwestward flow in the winter but northeastward flow in the summer in the western TWS as well as a northeastward flow in both the summer and winter in the eastern TWS. Chuang (1985) reported a mean northward current with occasional flow reversals in the TWS. The flow reversals were confirmed by Liang et al. (2003) based on shipboard acoustic Doppler current profiler (sb-ADCP) observations. Barotropic numerical models have been used to study the roles of the CYR, wind stress, and KBC in the TWS (Jan et al., 1994a, 1994b; Cai and Wang, 1997). The modeling results obtained by Jan et al. (1994b) indicated that the flow pattern around the CYR is determined mainly by the bottom topography and the inertial effect. The latter is associated with the incoming flows. Cai and Wang (1997) indicated that the

* Corresponding author. Tel.: +86-592-2185510; fax: +86-592-2185570.
E-mail address: ywjiang@xmu.edu.cn (Y. Jiang).

http://dx.doi.org/10.1016/j.ocemod.2016.04.006
1463-5003/

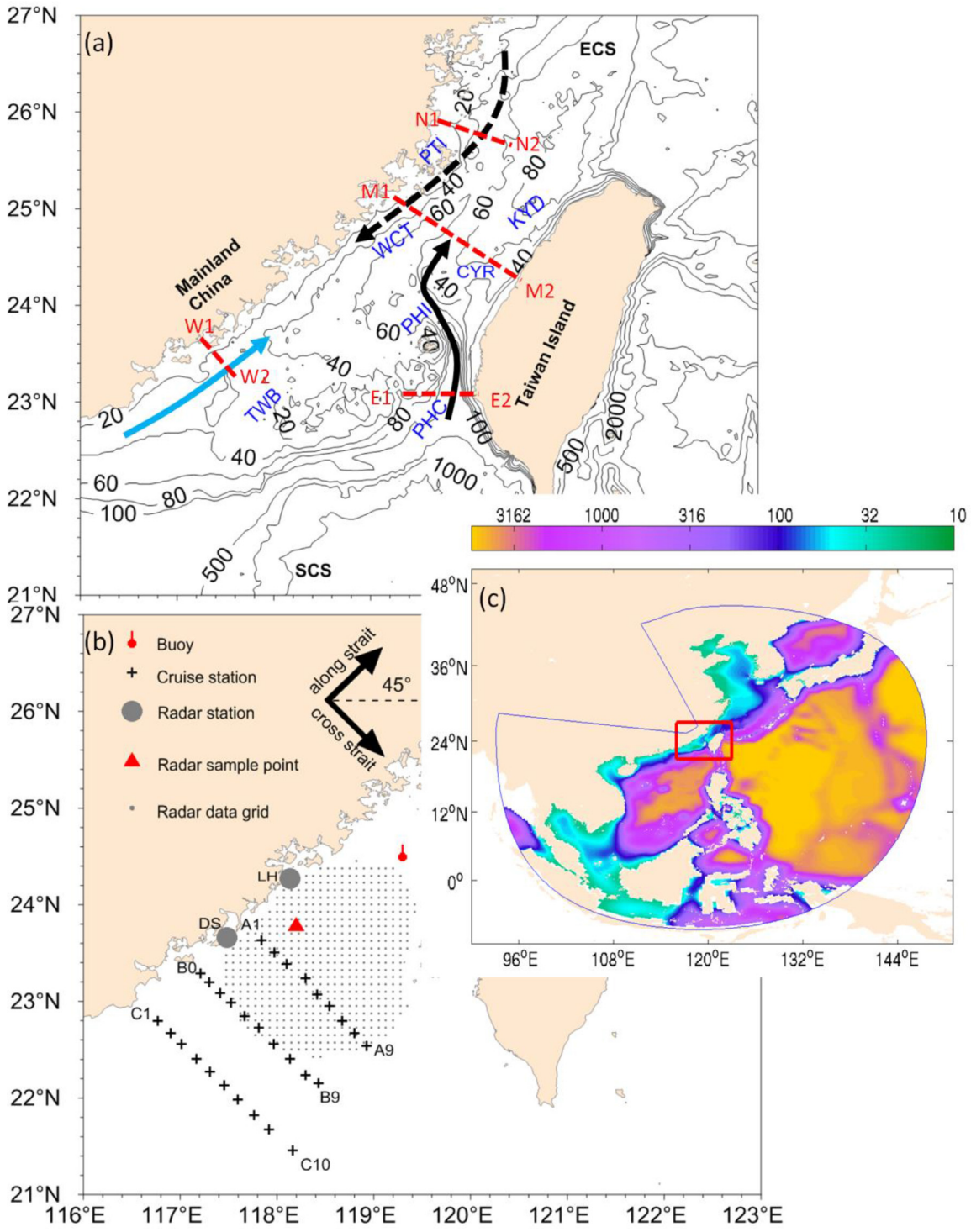

Fig. 1. Bottom topography (unit: m) of Taiwan Strait (a) and TFOR (c), and observations (b) in the Taiwan Strait. (a) SCS, ECS, KYD, WCT, CYR, TWB, PHI, PHC, and PTI denote South China Sea, East China Sea, Kuan-Yin Depression, Wuchou Trough, Changyun Ridge, Taiwan Bank, Penghu Island, Penghu Channel, and Pingtan Island, respectively. Zhemin Coastal Current (ZCC) is denoted by a dashed black arrow, Guangdong Coastal Current (GCC) by a solid blue arrow, and Kuroshio Branch Current (KBC) by a solid black arrow (combined with the extension of the SCS Warm Current). Dashed red lines indicate sections N1–N2, W1–W2, E1–E2, and M1–M2. (b) DS and LH denote two radar stations (gray solid circles) in Dongshan and Longhai with their coverage regions indicated by gray points. The red solid triangle denotes the radar sample point, where most radar velocities are available. The red mooring buoy is set at the center of the Taiwan Strait. Ship tracks are shown by the three black lines corresponding to stations A1–A9, B0–B9, and C1–C10 in June 2010. (c) The blue line delineates the TFOR domain and the red rectangle shows the location of panel (a).

wind, bottom topography, and Kuroshio current have great effects on the circulation in the TWS. The flow patterns in winter and summer were simulated by Jan et al. (1994b and 1998). The transport reversals during October and November 1999 were examined by Ko et al. (2003) using a real-time North Pacific Ocean model, and reexamined by Wu and Hsin (2005) with a 1/8° resolution hindcast model. Jan et al. (2004) showed that the reflection of the southward propagating tidal wave based on the deep trench in the southern strait is responsible for the complex wave propagation pattern. Wu et al. (2007) used modeling results to illustrate the transient, seasonal, and inter-annual variability of flows in the TWS. Zhu et al. (2008a) analyzed long-term measurements of

the surface flows obtained from a pair of high-frequency radar systems. Hu et al. (2010a) summarized the tidal wave behavior in the TWS and used a barotropic tidal model to examine the characteristics of the barotropic tides. In addition, Hu et al. (2010a) noted that the barotropic tidal waves dominated by semi-diurnal constituents in the Northwest Pacific Ocean essentially propagate westward to the ECS, where their amplitudes are magnified by quarter-wave resonance, and the associated barotropic tidal flows are exceptionally strong ($>1\,m\,s^{-1}$) along the northern coast of Taiwan and in the TWB. The strong tidal flows were also reported by Zhu et al. (2008a).

Several upwelling regions have been studied to assess their high fisheries production in the TWS. Four main upwelling regions were reviewed by Hu et al. (2003) and Hong et al. (2011a): Pingtan Island (PTI, shown in Fig. 1a), Dongshan (DS, shown in Fig. 1b), TWB, and Penghu Island (PHI, shown in Fig. 1a). Hu et al. (2003) stated that the first two are wind-driven with topographic forcing, whereas the other two are topographically induced. Numerical experiments by Jiang et al. (2011) showed that the ascending onshore current from the southwest is also a major driver of the DS upwelling and that strong tidal processes enhance vertical mixing in the TWB upwelling.

A salinity tongue that extends to the south of the TWB is another important hydrographical feature in the TWS, which was detected by Chen et al. (2002) based on the high sea surface temperature (SST) (up to 28.6°C) and low salinity (about 33 PSU). Hong et al. (2009) showed that the low salinity tongue is produced by Zhujiang diluted water, monsoon wind driving, coastal upwelling, and SCS Warm Current modifications.

The TWS volume transport is an important index of the water exchange between the ECS and SCS (Fu et al., 1991; Wang et al., 2003; Lin et al., 2005; Jan et al., 2006). Hu et al. (2010b) estimated the TWS volume transport as 2.3 Sv northward in summer and 0.8 Sv northward in winter. Liang et al. (2003) showed that the TWS volume transport is affected significantly by Kuroshio intrusion. Lin et al. (2005) concluded that variations in TWS volume transport are correlated strongly with the changes in the along-PHC sea level gradients as well as monsoonal winds. Chuang (1985) proposed a momentum balance among the wind stress, mean current, and pressure gradient between the north and south of the TWS. Numerical experiments by Wu and Hsin (2005) showed that the pressure gradient forces a mean current northward year round. Wu and Hsin (2005) also reported good agreement between the transport obtained from their simulation and that based on Chuang's equation.

Research projects, such as Nowcast System for the TWS (Jan et al., 2001) and Strait Watch on the Environment and Ecosystem with Telemetry (Chen, 2004), have played crucial roles in understanding the flow patterns in the TWS. Jan et al. (2001) developed an operational tidal model and obtained good agreement between their modeling results and observations, as well as providing co-tidal charts and depth-averaged tidal velocity ellipses for the calculated M_2 tide in the TWS. Advanced Taiwan Ocean Prediction is another operational model (Oey et al., 2013), which focused on the currents near Taiwan Island, but it did not consider the tides or river discharge. In the present study (Fujian Coastal Monitoring System Project), we aimed to develop a real-time ocean observation system for the TWS and adjacent maritime regions. One of the goals was to develop the TWS Nowcast/Forecast System (TFOR) by considering the circulation, tide, and river discharge. The TFOR provides hindcast and forecast products, including temperature, salinity, and velocity, thereby enhancing our understanding of the major physical processes in the TWS, such as the monsoon, tide, and upwelling. Previous model sensitivity tests by Jiang et al. (2011) have shown that tidal mixing can diffuse the subsurface cold water to form upwelling in the TWB. In addition, for upwelling off PTI, the tide can alter the upwelling location through a tidal mixing effect (Chen et al., 2014).

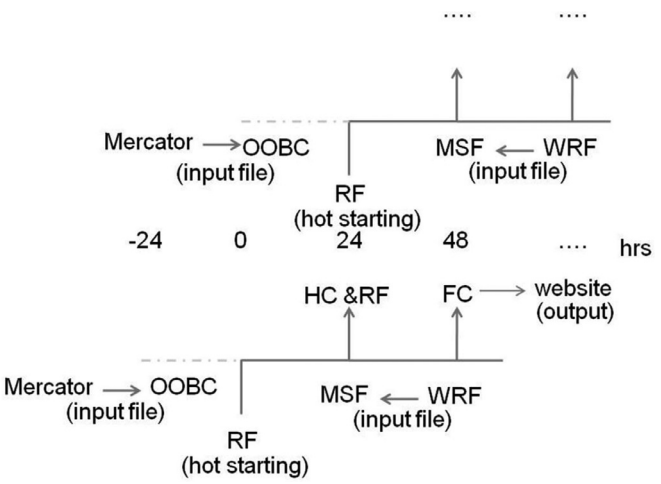

Fig. 2. Schema of the TFOR framework. 24-h hindcasts and 48-h forecasts are produced daily by intermittent simulation based on the re-starting file. Surface forcing is provided by an operational weather research and forecast model (WRF) and open ocean boundary conditions are obtained from Mercator products. OOBC, MSF, RF, HC, and FC represent an ocean open boundary condition, marine surface forcing, re-starting file, hindcasts, and forecasts, respectively.

In this study, we conducted a performance assessment for the TFOR. The following section describes the configuration of TFOR. In Section 3, we introduce the various types of observational data that are available. In Section 4, we compare the observational data and the TFOR results in detail. In Section 5, we provide a brief summary and give our conclusion.

2. Model system

2.1. Model configuration

The Regional Ocean Modeling System (Shchepetkin and McWilliams, 2003, 2005) is a free surface, terrain-following, primitive equation ocean model, which is capable of producing high-resolution descriptions of coastal and basin-wide flows. The modeling domain delineated in Fig. 1c covers the northwestern Pacific Ocean with curvilinear grids. The variable horizontal resolution ranges from approximately 45 km at the open boundary to 1.5 km in the TWS. There are 30 vertical layers, which are derived by a stretching function with $\theta_s = 3.0$, $\theta_b = 0.4$, and $h_c = 10$ m, as developed by Song and Haidvogel (1994). The model is configured with fourth-order centered horizontal advection of momentum and tracers with a mixing scheme (Large et al., 1994). The Flather boundary condition (Flather, 1976) and Chapman boundary condition (Chapman, 1985) are applied in the model for the two-dimensional velocity and elevation, respectively.

The model bathymetry is merged with 25 digitized ocean charts published by the Maritime Safety Administration (China), the TWS 0.5′ gridded bathymetry (http://www.odb.ntu.edu.tw), and ETOPO2v2 from the National Geophysical Data Center (https://www.ngdc.noaa.gov). In terms of the cruise observation depth (introduced in Section 3, Figs not shown), the ocean chart depth is more accurate than ETOPO2v2 in the coastal region. To reduce the unexpected diapycnal mixing error, a weak filter is applied to smooth the bathymetry (Mellor et al., 1998).

The air-sea flux data, e.g., the wind speed, surface downward short-wave and long-wave radiation, sea level pressure, and freshwater flux, are interpolated from a 0.2° resolution weather research and forecast model (WRF) supported

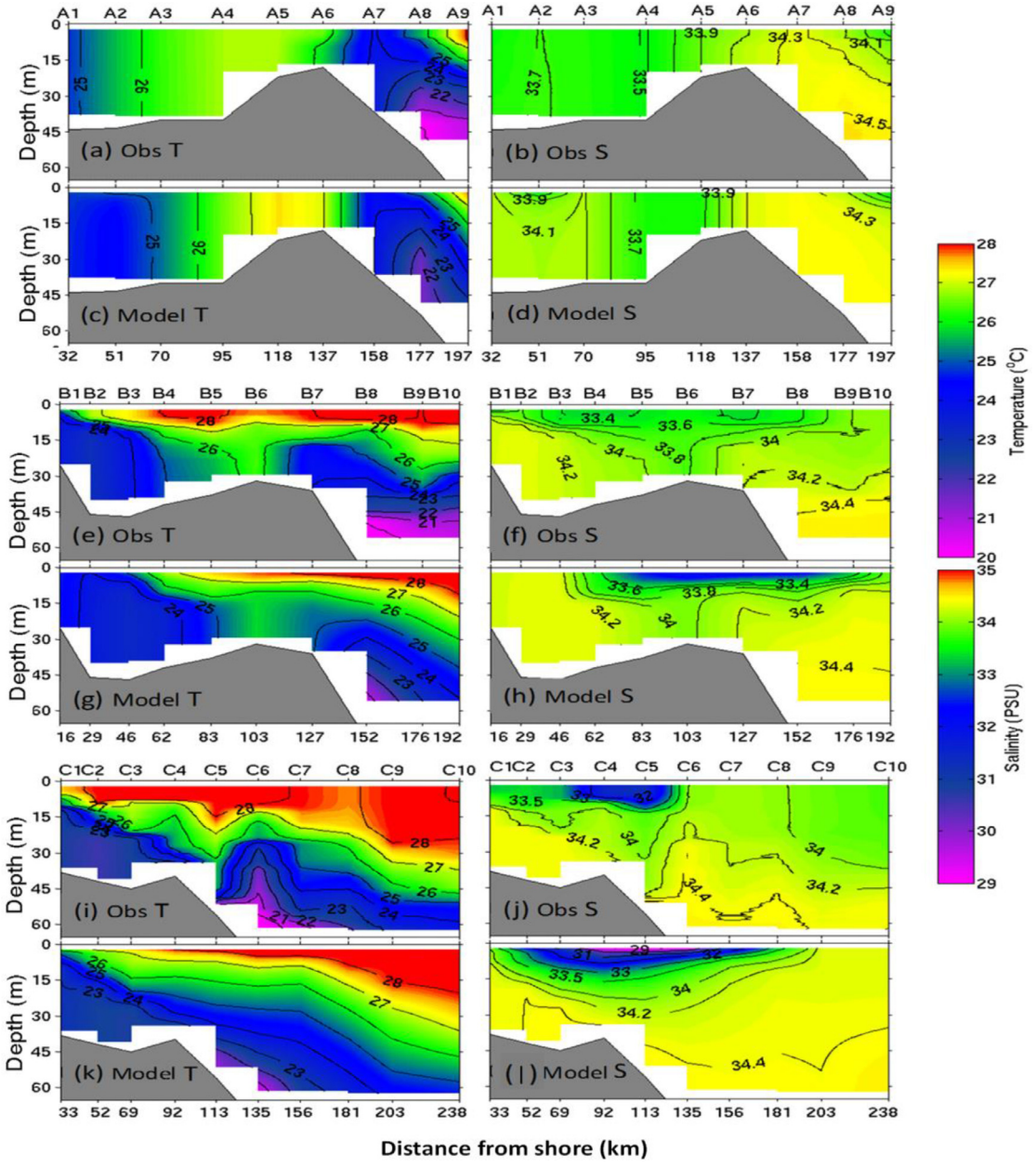

Fig. 3. Comparison of the snapshot temperature (unit:°C) and salinity (unit: PSU) according to the model results and shipboard measurements. The measurements were performed during June 22–26, 2010.

by the National Marine Environmental Forecasting Center (http://www.nmefc.gov.cn/szyb/fc.aspx). These parameters are treated as the sources in the vertical viscosity/diffusion terms of the momentum and tracer equations, and they are implemented in the model as surface forcing. In addition, the surface net heat flux is adjusted with the net heat flux sensitivity to the climatological SST, thereby avoiding large deviations in the SST from its normal range in long-term simulations. Killworth et al. (2000) assumed that the surface temperature is produced by a combination of surface forcing and advective forcing, which satisfies

$$\frac{\partial T_M}{\partial t} = \frac{(T - T_M)}{\tau} + F_A(t, T_M), \tag{1}$$

where T_M is the model SST, T the climatological SST, τ is the relaxation coefficient pulling T_M to T, and F_A is the advective forcing for the SST. τ is set to 90 days in TFOR. The Comprehensive Ocean-Atmosphere Data Set SST (http://iridl.ldeo.columbia.edu/SOURCES/.COADS) is taken as the climatological SST in the TFOR.

Tidal forcing at the lateral boundary is deduced from TPXO7.0 (Egbert and Erofeeva, 2002) with 10 main tidal components (M_2, S_2, N_2, K_1, K_1, O_1, P_1, Q_1, M_f, and M_m). The monthly mean discharges from the major rivers (Chen, 1994) along the mainland coast are considered in the model. These rivers include the Yangtze River, Pearl River, Yalu River, Liaohe River, Luanhe River, Ou River, Minjiang River, Jiulong River, and Hanjiang River. The parameters at the lateral boundary, e.g., sea level, velocity, temperature, and salinity, are derived from Mercator products (http://www.mercator-ocean.fr, 2008, http://myoceans.com, 2013) as well as the initial parameters on August 1, 2007. As an operational model, 24-h hindcasts and 48-h forecasts are provided automatically on a daily basis. The TFOR has been applied in several previous studies, where Liao et al. (2013) proposed a mechanism for the cold disaster during February 2008 in the TWS,

Wang et al. (2013) developed a coupled physical-biological model for the TWS, and Lu et al. (2015) proposed a mechanism for the Luzon bloom.

2.2. Model operation

Daily operation includes three processes: pre-processing, simulation (hindcast and forecast), and post-processing. The TFOR framework is shown in Fig. 2. These processes are conducted automatically via scripts. Pre-processing prepares the ocean open boundary files from Mercator products and marine surface forcing files from the WRF model. Both require the interpolation of variables onto the TFOR model grids. Tests by Zhang (2009) indicated that the prediction error during the first 48-h was close to the simulation error in the assimilation stage of the TFOR. Therefore, 72-h simulation products are renewed every day, including 24-h hindcasts and 48-h forecasts. It is permissible to treat the simulation performance as the prediction performance. The scenario that connects the hindcasts and forecasts is maintained as the re-starting file for the hot-starting simulation on the next day. This re-starting file strategy has some advantages because the system can be recovered easily in the case of failure from the most recent correct re-starting file.

3. Observations

Three types of observational data were collected to evaluate TFOR: short-term *in-situ* ship investigations, remote sensing data, and the Fujian Coastal Monitoring System Project (Jiang et al., 2007). One of the short-term *in-situ* investigation datasets comprised the conductivity, temperature, and depth sensor data observed by R/V Yanping No. 2 during June 22–26, 2010, with three sections of hydro-cast stations, i.e., A1–A9, B0–B9, and C1–C10, as shown in Fig. 1b, and cast depths limited to the upper 70 m. Another short-term *in-situ* observational dataset was obtained from the sb-ADCPs (307.2 kHz, and bin size of 1.0 m) deployed in the southern TWS (indicated by red ellipses 3 and 4 in Fig. 7), where dramatic variations in tidal flow occurred. Measurements were conducted near Station A8 (C5) during July 2–11 (11–18), 2012. The daily remote sensing SST data obtained by the Moderate-resolution Imaging Spectroradiometer (MODIS) were collected from the ocean color website (http://oceandata.sci.gsfc.nasa.gov/MODIST, 2013) with a spatial resolution of 4 km, which is similar to the TFOR grid resolution in the TWS. The Fujian Coastal Monitoring System Project provided two types of current velocities: the sea surface current from the Ocean State Measuring and Analyzing Radars and vertical current profiles from buoy-mounted ADCPs (bm-ADCPs). Two radar systems were deployed in the DS and Long-hai (LH, shown in Fig. 1b), which operated at a frequency of 7.8 MHz, to monitor the currents at a 10-min time interval in the southwestern TWS (Zhu et al., 2008a). Validation based on comparisons of multi-ship observations showed that the root mean-squared errors of the radar current components were generally between 0.07 and 0.2 m s^{-1}, where larger errors occurred in the area far from the radar, whereas the sample points in the coverage area (e.g., the solid triangle shown in Fig. 1b) had the most accurate data (Zhu, 2008b). The bm-ADCPs in the central and northern part of the TWS (buoy in Fig. 1b and red ellipse 2 in Fig. 7) measured the velocity profiles in the depth range from 5.5 m to 50.5 m at an interval of 5 m.

4. Model assessment

4.1. Model performance

Multiple statistical metrics were used to perform the model–data comparisons. The mean bias (MB) measures the mean difference between the observational data and the TFOR results. The correlation coefficient (CC) describes the colinearity between their time series. The root mean-squared difference (RMSD) is an absolute measure of the distance between the observational data and the TFOR results. The Willmott skill (WS; Willmott, 1981; Liu et al., 2009) is a simple measure for quantifying the extent to which the TFOR results agree with the observational data, where the *WS* varies from 0 to 1: $WS=1$ indicates perfect agreement between the observational data and the TFOR results, whereas $WS=0$ indicates no agreement at any point. These statistics are defined as follows:

Table 1
Model performance metrics for different variables.

Variable	MB	RMSD	CC	WS
Cruise T	−0.01 °C	1.2 °C	0.87	0.92
Cruise S	0.06 PSU	0.4 PSU	0.74	0.83
SST Feb/2008	0.10 °C	1.53 °C	0.95	0.97
SST winter	0.55 °C	0.71 °C	0.99	0.99
SST summer	−0.22 °C	0.49 °C	0.93	0.92
Detided ADCP U	0.07 m s^{-1}	0.13 m s^{-1}	0.03	0.41
Detided ADCP V	0.03 m s^{-1}	0.14 m s^{-1}	0.81	0.88
Radar centre U	0.02 m s^{-1}	0.12 m s^{-1}	0.77	0.86
Radar centre V	−0.08 m s^{-1}	0.19 m s^{-1}	0.91	0.94
Detided radar centre U	0.02 m s^{-1}	0.06 m s^{-1}	0.34	0.59
Detided radar centre V	−0.07 m s^{-1}	0.14 m s^{-1}	0.73	0.87
Detided radar winter U	−0.001 m s^{-1}	0.03 m s^{-1}	0.77	0.76
Detided radar winter V	−0.06 m s^{-1}	0.08 m s^{-1}	0.76	0.58
Detided radar summer U	0.03 m s^{-1}	0.06 m s^{-1}	0.58	0.70
Detided radar summer V	0.08 m s^{-1}	0.13 m s^{-1}	0.11	0.26

$$MB = \langle m - o \rangle, \tag{2}$$

$$CC = \frac{1}{n}\sum_{i=1}^{n}(m_i - \langle m \rangle)(o_i - \langle o \rangle)/(\sigma_m \sigma_o), \tag{3}$$

$$RMSD = \left[\frac{1}{n}\sum_{i=1}^{n}(m_i - o_i)^2\right]^{1/2}, \tag{4}$$

$$WS = 1 - \frac{\langle (m-o)^2 \rangle}{\langle (|m - \langle o \rangle| + |o - \langle o \rangle|)^2 \rangle}, \tag{5}$$

where m and o are the time series (n) for the modeled and observed variables, respectively, and σ_m and σ_o are their respective standard deviations. Angled brackets $\langle\,\rangle$ denote a mean operator and n is the number of observational samples. In addition, a type of non-dimensional skill score (*SS*) was considered. Kara et al. (2008) used the SS to measure the difference between the Modular Ocean Data Analysis System and HYCOM SST, and it is expressed as follows:

$$B_{\text{cond}} = [CC - (\sigma_m/\sigma_o)]^2, \tag{6}$$

$$B_{\text{uncond}} = [(\langle m \rangle - \langle o \rangle)/\sigma_o]^2, \tag{7}$$

$$SS = CC^2 - B_{\text{cond}} - B_{\text{uncond}}, \tag{8}$$

where B_{cond} is the conditional bias due to the differences in the standard deviations, which measures the relative amplitude of the variability in the MODIS and TFOR SST time series, and B_{uncond} is the unconditional bias, which is also called the systematic bias. SS can reach as up to 1.0 for perfect simulations, whereas a negative value indicates a poor simulation.

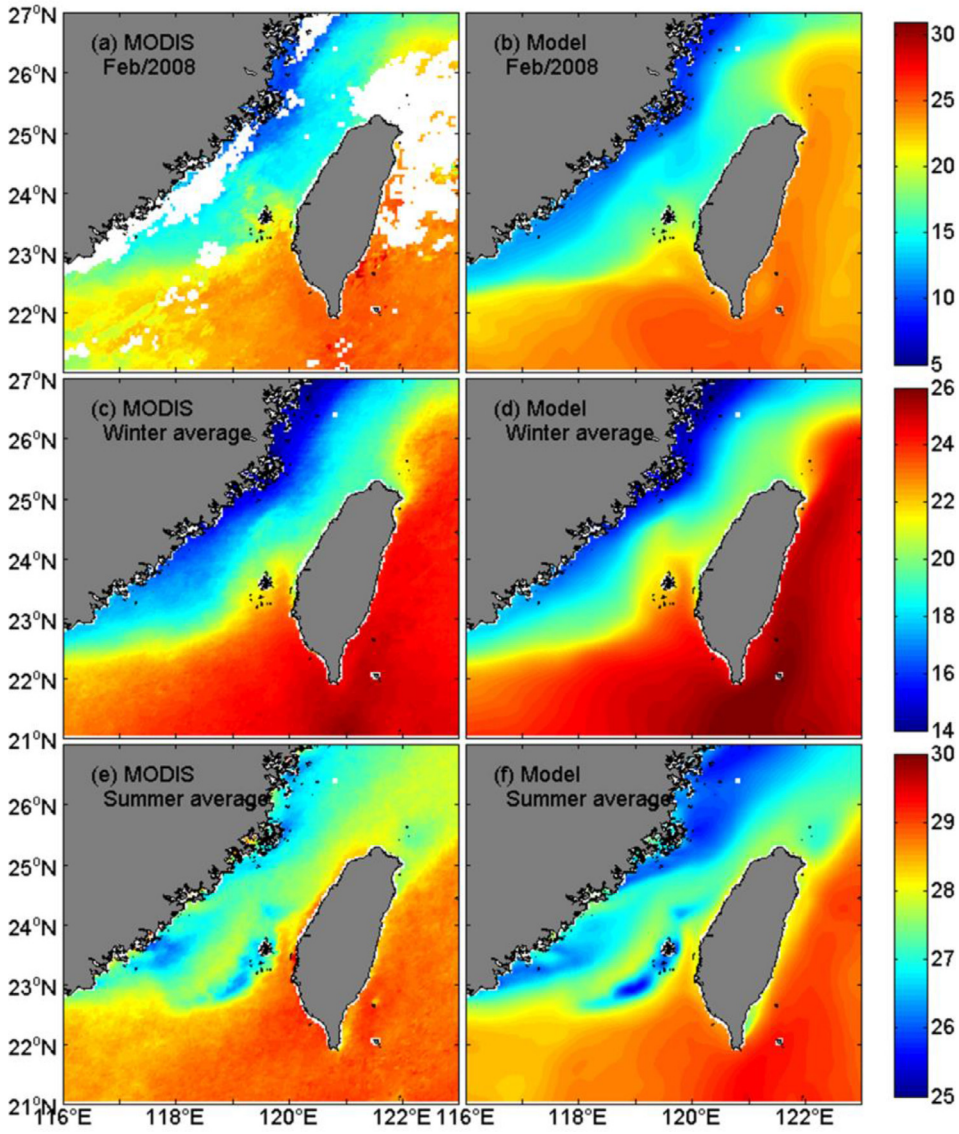

Fig. 4. Monthly averaged SST (unit:°C) for February, 2008 and SST patterns for winter and summer based on MODIS measurements and model results. Winter refers to December, January, and February during 2009–2012, and summer refers to June, July, and August during 2009–2012.

4.2. Tracer comparison

The cruise data described in Section 3 indicate some important characteristics of the summertime seawater properties in the TWS (Fig. 3). Figs 3a, 3b, 3c, and 3d represent well-mixed water in the vertical direction from A3 to A6, thereby indicating strong tidal mixing in the TWB. Upwelling in the TWB was characterized by a low temperature of 22°C (Figs 3a and 3c) and a high salinity of 34.3 PSU (Figs 3b and 3d) at Station A8. However, weak stratification was found at Station A2 in the model (Fig. 3d), whereas the observations (Fig. 3b) indicated a well-mixed pattern. This difference may be explained by an inaccurate input for the river flux that flows into the TWS near the south of the DS. The contours in Figs 3e, 3f, 3g, and 3h show that the water mass with low salinity and high temperature between B5 and B7 is sandwiched between coastal and deep waters with lower temperature and higher salinity. The model temperature (Fig. 3k) exhibited a similar stratification pattern to the observations (Fig. 3i), except the observed upwelling at the continental slope near C6 (not reported before this study) was not resolved in the model (Fig. 3k). This upwelling is also shown in Fig. 3j, but not in Fig. 3l. Jiang et al. (2011) investigated the characteristics and underlying mechanism of the upwelling in the TWS, and discussed the contributions of upwelling from upslope advection and strong tidal processes. Gan et al. (2015) found that a favorable pressure gradient force for upwelling and the bottom frictional effect in the prominent eastward widened shelf could sustain upwelling during episodic favorable winds for downwelling. This upwelling may be related to either internal waves that cannot be implemented in TFOR under an assumption of static pressure, or the complex bottom topography at the continental slope near C6 which cannot be resolved accurately at the model's spatial resolution. The low salinity band was wider in the model (Fig. 3l) than that in the observations (Fig. 3j), but the diluted water patterns were quite similar. Hong et al. (2009) described the three-dimensional (3-D) structure of the low salinity tongue using cruise data from June 2005 and showed that it was derived from the Pearl River Estuary. The statistical analyses (Table 1) showed that the MB, RMSD, CC, and WS for the differences in temperature between the cruise data and model results were –0.01°C, 1.2°C, 0.87, and 0.92, respectively, and those corresponding to the salinity were 0.06 PSU, 0.4 PSU, 0.74, and 0.83, respectively. This comparison of the cruise data

Table 2
Comparison of the tidal harmonic constants at tide-gauge stations. A represents the amplitude (unit: m), and G represents the phase (unit: °). The reference time for the phase is Greenwich Mean Time (GMT). The observational results are shown below the model data.

St.			O_1		K_1		M_2		S_2	
No.	N.	E.	A	G	A	G	A	G	A	G
1	21.97	120.75	0.19	78	0.22	136	0.27	310	0.13	327
			0.18	93	0.25	141	0.26	306	0.11	332
2	22.07	120.68	0.19	95	0.18	164	0.21	322	0.11	329
			0.17	116	0.24	161	0.20	319	0.10	342
3	22.47	120.45	0.18	104	0.16	175	0.25	342	0.10	348
			0.16	127	0.25	188	0.18	353	0.07	351
4	22.62	120.27	0.17	100	0.17	170	0.18	343	0.08	341
			0.15	129	0.26	174	0.16	355	0.06	7
5	22.98	120.15	0.18	94	0.19	166	0.23	33	0.06	28
			0.15	128	0.28	169	0.20	28	0.07	51
6	23.10	120.07	0.19	96	0.21	165	0.35	64	0.08	85
			0.18	116	0.30	158	0.29	55	0.04	90
7	23.43	120.15	0.20	95	0.18	164	0.76	80	0.21	112
			0.18	117	0.31	158	0.61	71	0.15	124
8	23.70	120.17	0.21	96	0.21	164	1.17	91	0.34	125
			0.15	115	0.31	153	1.13	91	0.24	139
9	23.92	120.30	0.22	95	0.18	162	1.50	95	0.45	128
			0.21	115	0.18	153	1.43	90	0.34	139
10	24.18	120.48	0.22	94	0.12	161	1.71	96	0.53	128
			0.15	102	0.20	148	1.49	86	0.37	135
11	22.03	121.57	0.13	80	0.12	139	0.41	303	0.18	323
			0.12	86	0.21	122	0.46	291	0.21	335
12	22.67	121.48	0.13	69	0.15	131	0.41	301	0.19	320
			0.12	71	0.19	111	0.43	282	0.18	330
13	22.83	121.18	0.14	68	0.15	132	0.41	302	0.18	319
			0.15	73	0.21	112	0.43	285	0.18	311
14	23.12	121.40	0.13	69	0.18	124	0.43	301	0.20	322
			0.12	70	0.22	99	0.52	283	0.21	321
15	24.58	121.87	0.15	67	0.25	131	0.37	299	0.18	319
			0.18	69	0.18	103	0.43	285	0.18	319
16	25.15	121.75	0.15	72	0.20	133	0.19	33	0.07	7
			0.15	75	0.18	108	0.19	40	0.05	38
17	24.62	120.75	0.21	92	0.30	157	1.69	94	0.53	124
			0.18	92	0.21	133	1.64	86	0.49	124
18	25.18	121.43	0.17	84	0.24	147	0.76	86	0.23	110
			0.18	86	0.21	127	1.00	76	0.30	116
19	23.22	119.42	0.21	99	0.29	168	0.52	102	0.13	142
			0.21	130	0.24	166	0.55	90	0.12	140
20	23.37	119.52	0.21	99	0.29	168	0.71	102	0.19	140
			0.21	118	0.21	157	0.61	85	0.12	137
21	23.55	119.55	0.22	99	0.31	168	1.01	106	0.29	142
			0.21	116	0.24	158	0.88	87	0.24	136
22	23.73	119.60	0.22	99	0.32	167	1.26	105	0.38	141
			0.21	117	0.21	159	1.22	93	0.30	156
23	22.82	116.10	0.25	102	0.38	173	0.08	11	0.06	348
			0.21	131	0.37	176	0.15	83	0.09	128
24	22.93	116.48	0.24	102	0.37	173	0.10	140	0.04	286
			0.21	231	0.37	177	0.24	127	0.09	177
25	23.33	117.75	0.25	103	0.37	173	0.85	132	0.25	178
			0.24	130	0.30	176	0.43	146	0.09	210
26	23.47	117.02	0.25	105	0.38	175	0.61	149	0.18	202
			0.27	131	0.30	176	0.70	148	0.15	208
27	23.75	117.28	0.25	104	0.38	175	0.92	145	0.28	194
			0.30	131	0.34	175	0.76	139	0.18	205
29	24.38	118.17	0.26	100	0.39	169	1.90	122	0.60	160
			0.18	127	0.27	158	1.86	120	0.40	184
30	24.38	118.07	0.26	101	0.39	169	1.83	123	0.58	161
			0.18	127	0.27	159	1.98	123	0.46	187
31	24.38	118.57	0.26	97	0.38	165	1.92	114	0.61	150
			0.18	121	0.27	147	1.98	110	0.46	170
32	24.38	118.72	0.26	95	0.38	162	2.16	109	0.69	143
			0.18	125	0.27	147	2.01	120	0.55	175
33	24.38	119.05	0.26	93	0.38	160	2.33	105	0.75	139
			0.21	109	0.27	127	2.04	89	0.61	139
34	24.38	119.58	0.25	88	0.36	154	2.25	95	0.73	126
			0.21	102	0.27	116	2.07	79	0.67	126
35	24.38	119.68	0.23	78	0.34	143	2.15	79	0.72	107
			0.21	98	0.27	114	2.10	69	0.67	117
36	24.38	119.92	0.22	77	0.33	141	1.99	75	0.67	102
			0.21	95	0.30	112	2.13	58	0.70	105
37	24.38	119.63	0.23	76	0.34	140	2.18	74	0.73	102
			0.24	98	0.27	134	2.04	74	0.58	119
38	24.38	119.92	0.22	76	0.33	140	2.02	73	0.68	100
			0.21	85	0.30	114	2.25	53	0.79	100
39	26.50	120.05	0.22	73	0.33	137	2.03	66	0.70	93
			0.21	80	0.30	112	2.13	50	0.73	97
40	26.63	119.70	0.22	97	0.33	161	2.36	109	0.76	147
			0.24	82	0.34	126	2.56	62	0.79	108
41	25.68	119.58	0.23	81	0.35	146	2.21	84	0.74	114
			0.25	89	0.31	122	2.22	68	0.66	109
42	25.47	119.83	0.23	83	0.35	149	2.04	87	0.67	117
			0.25	92	0.31	131	2.04	71	0.62	113
43	25.42	119.12	0.25	90	0.38	157	2.48	100	0.80	133
			0.25	103	0.28	142	2.46	97	0.69	143
44	24.45	118.07	0.26	101	0.39	169	1.83	123	0.58	161
			0.28	120	0.34	163	1.83	116	0.53	169
45	23.73	117.53	0.25	105	0.38	174	1.11	141	0.34	185
			0.26	126	0.32	171	1.05	130	0.29	188
46	26.17	119.95	0.22	75	0.33	139	1.99	71	0.68	98
			0.25	88	0.31	120	2.10	64	0.66	96
47	24.98	119.45	0.25	90	0.36	157	2.11	98	0.67	131
			0.25	112	0.39	147	2.05	89	0.55	126
48	25.30	121.60	0.17	79	0.23	141	0.39	79	0.10	92
			0.18	92	0.21	116	0.47	73	0.12	92
49	25.18	121.40	0.17	85	0.24	149	0.83	89	0.25	114
			0.18	97	0.20	126	0.99	80	0.30	112
50	24.85	120.92	0.20	90	0.29	155	1.60	93	0.50	121
			0.20	106	0.23	134	1.61	85	0.47	118
51	24.33	120.55	0.21	94	0.31	161	1.75	96	0.54	127
			0.20	115	0.24	145	1.73	90	0.50	123
52	23.67	120.13	0.21	96	0.30	164	1.11	91	0.32	125
			0.20	125	0.23	157	1.00	81	0.28	119
53	23.38	120.15	0.20	95	0.28	164	0.71	80	0.19	112
			0.19	126	0.21	161	0.63	75	0.16	107
54	23.25	119.67	0.20	97	0.28	167	0.49	91	0.12	127
			0.19	125	0.20	159	0.50	79	0.10	112
55	22.62	120.28	0.17	100	0.24	170	0.19	343	0.08	341
			0.16	129	0.18	167	0.18	351	0.07	353
56	21.95	120.75	0.19	78	0.27	136	0.28	310	0.13	327
			0.20	105	0.22	134	0.26	312	0.11	323

and modeling results indicates that the accuracy of the model is acceptable for reproducing the tracer patterns, and that the temperature was simulated better than the salinity due to the uncertainty in the river freshwater flux.

In this study, the comparisons between MODIS and the TFOR SST focused on the cold disaster in February 2008 (Chang et al., 2009; Liao et al., 2013) and the average SST patterns during winter and summer (Fig. 4). Fig. 4a shows an averaged composite of the MODIS SST products, Terra and Aqua. The data gaps in Fig. 4a correspond to severe contamination of the MODIS SST by winds and clouds along the Chinese coastal area, and to the northeast of Taiwan Island during February 2008. It is evident that the low temperature (<10°C) related to the China Coastal Current (CCC) was dominant in the northwestern TWS and that the high temperature (>20°C) was located in the southern TWS and east of Taiwan Island due to the Kuroshio water. It should be noted that the temperature transition occurred in the middle of the TWS, and that the low-temperature tongue stretched from PTI toward PHI in February 2008. Using this model, Liao et al. (2013) investigated the underlying mechanism of this disaster and divided the disaster processes into three stages: offshore extension, southwestward intrusion, and northeastward retreat. The monthly averaged SST from the TFOR (Fig. 4b) shows that warm water (>20°C) was present off the eastern and southern coasts of Taiwan Island, whereas cold water (<10°C) dominated the coast off mainland China. The SST front (indexed by 14°C) delineated a cold temperature tongue in the middle part of the TWS, which directly faced the warm temperature tongue near PHI originating from the KBC. Compared with Fig. 4a, the TFOR results (Fig. 4b) illustrated the situation of the cold disaster during February 2008 in a clearer and smoother manner. The statistical analyses (Table 1) show that the calculated MB, RMSD, CC, and WS between the MODIS SST and the TFOR results were 0.10°C, 1.53°C,

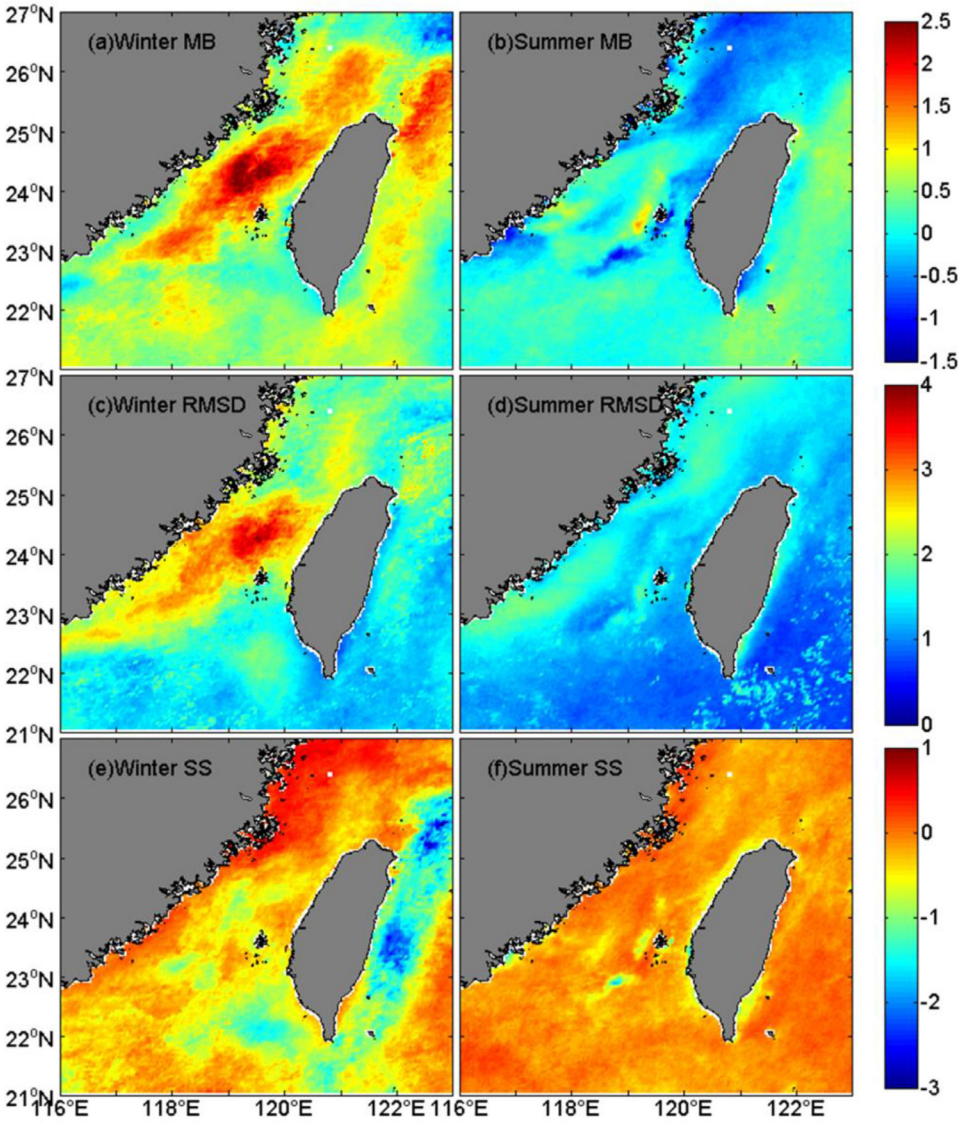

Fig. 5. MB (unit:°C), RMSD (unit:°C), and SS for winter and summer SST patterns obtained from the model and MODIS.

0.95, and 0.97, respectively. Thus, the SST comparison showed that TFOR can reproduce the SST pattern when dramatic changes occur.

The winter and summer patterns of the SST in the TWS are quite different due to the monsoons. Figs 4c and 4d show the winter mean SST obtained from MODIS and TFOR (December, January, and February during 2009–2012). The winter mean SST in Fig. 4d is similar to that in February 2008 (Fig. 4b), except for the cold water intruding southward from PTI to PHI, which makes the water temperature in PHI as low as 15°C in Fig. 4b compared with approximately 22°C in Fig. 4d. This 7°C difference is consistent with the observations (7.8°C), as mentioned above. A slight difference is visible between Fig. 4c and 4d, but the fronts of the cold and warm water masses in MODIS are not as sharp as those in the model. The CC and WS between MODIS and the model are both 0.99 (Table 1) in the winter. Figs 4e and 4f show the summer mean SST (June, July, and August during 2009–2012) obtained from MODIS and the model. A low SST can be seen in the upwelling regions, e.g., at the TWB, off the DS, PTI, and north of Taiwan Island. The warm SST is seen along the southwestern coastal regions of Taiwan Island, thereby indicating that the KBC flows northward through the PHC, which is consistent with the description given by Jan et al. (2002).

Other aspects of the model's performance were demonstrated by further comparisons. Figs. 5a and c show that the largest MB and RMSD values were 1.5 and 3°C (the averaged values are 0.55 and 0.71°C in Table 1), respectively, which were both found in the central axis of the TWS. This finding is attributable to the modulation of the CCC and KBC under unsteady northeasterly winds during the winter (Jan et al., 2003; Liao et al., 2013). For the summer pattern, both the MB and RMSD showed that the major difference occurred around the upwelling regions. A high SS value was found over almost the entire TWS during the summer (Fig. 5f). However, SS values lower than −1 were found to the east and south of Taiwan Island during the winter (Fig. 4e). In these regions, the MODIS SST time series were unable to represent the actual trend because of gaps in the data. The seasonal SST patterns in the TWS obtained from the TFOR were comparable to those from MODIS. The difference in the SST between the TFOR and MODIS may be attributable to accuracies in the MODIS data and surface forcing in the TFOR.

4.3. Tide information

The Matlab tools tide package (Pawlowicz et al., 2002) was used to calculate the tidal elevation harmonic constants (Fig. 6) and current ellipse (Fig. 7) for the M_2 tide. Fig. 6 shows that the maximum amplitude (approximately 2 m) of the M_2 tide occurred at PTI. Tiny amplitude gradients were found in the southern TWS

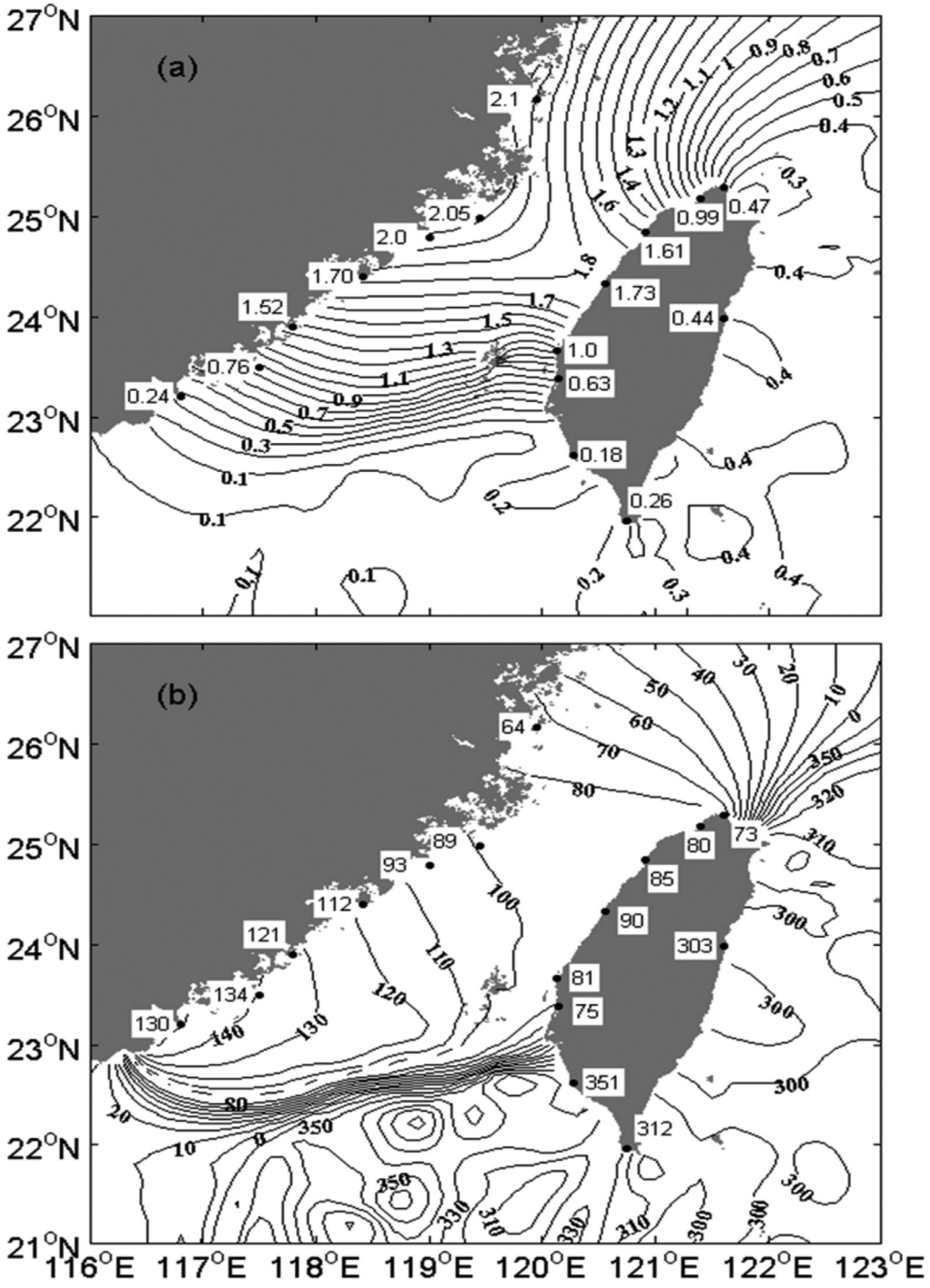

Fig. 6. Comparison of M_2 tide harmonic constants, amplitude (a, unit: m), and phase (b, unit: °) in the Taiwan Strait. The contours indicate the model results and the dots represent tidal gauge stations.

and east of Taiwan Island, where the water depth is approximately 3000 m. Fig. 6b shows that the M_2 wave originates from the Northwest Pacific Ocean, propagates into the TWS, reaches the TWB, and is reflected by the continental slope off the TWB, thereby resulting in the maximum amplitude of the M_2 near PTI (Jan, 2004). The RMSDs in the amplitude and phase between the observations and TFOR were 0.10 m and 11.57°, respectively. The maximum difference occurred along the western coast of Taiwan Island, i.e., 20.76° for the phase in the middle and 0.19 m in amplitude across PHI and near the northern tip of Taiwan Island. Overall, the distributions of the M_2 harmonic constants are consistent with the results given by Jan (2004), Hu et al. (2010a), and Jiang et al. (2011), thereby indicating similar tidal characteristics.

The tidal current in the TWS is complex. Fig. 7 shows the distribution of M_2 tidal ellipses obtained from the TFOR results in black and those acquired from the available ADCP observations in red. The tidal currents are weak in the deep western part of the Pacific Ocean and they become stronger on the shallow shelf of the ECS. Moreover, the major axes of the tidal ellipses are aligned almost exactly with the coast of the TWS, except at the northern reaches of the TWS where they align zonally. Clearly, a dramatic variation in the tidal currents occurs in the TWS. The strongest

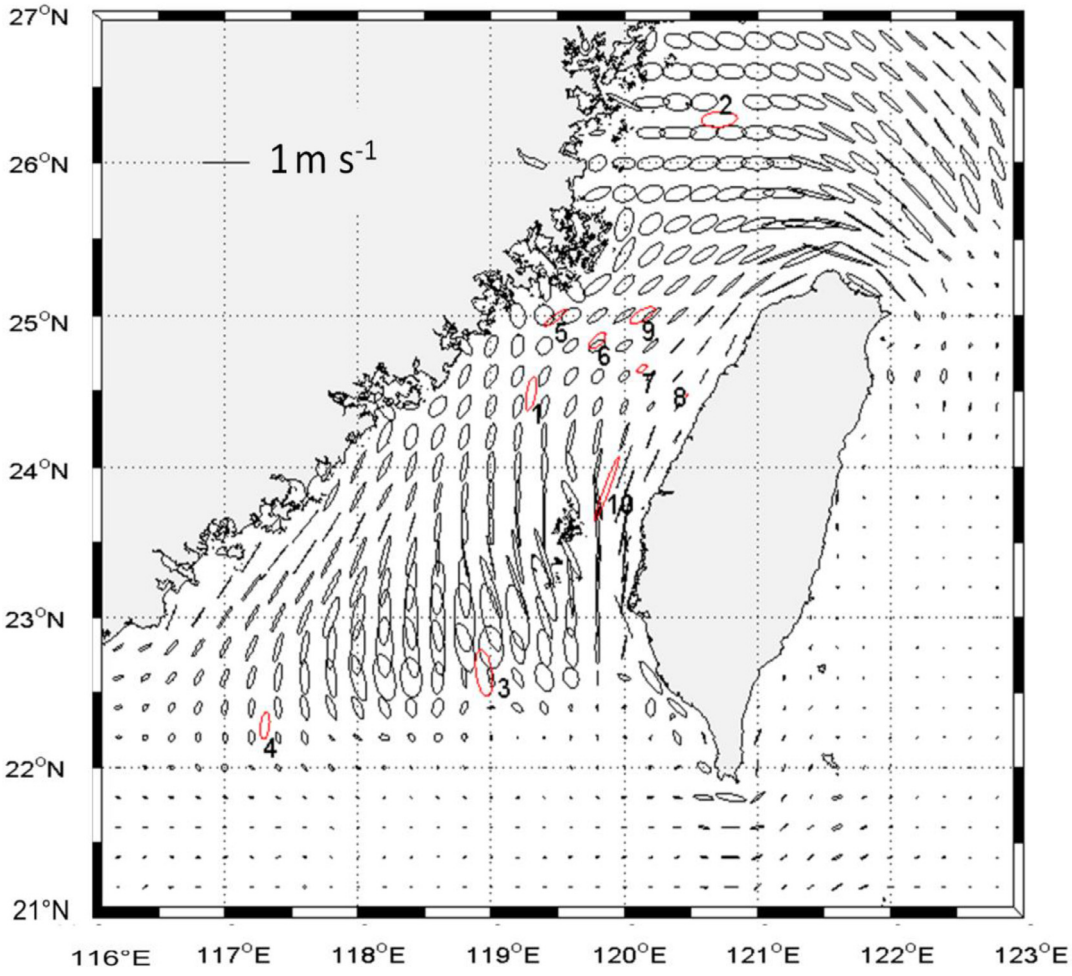

Fig. 7. Tidal ellipses of M_2 where the modeling results are displayed in black and observations at the 10 stations in red.

M_2 tidal currents occur in the southern section of the TWS, i.e., the shallow TWB (approximately 20 m depth), and the weakest in the middle section, while the northern section has intermediate strength tidal currents. In addition, it should be noted that the M_2 tidal currents are very weak south and east of Taiwan Island, where the depth is greater than 1000 m, except for those near the southern and northern tips of Taiwan Island due to the nonlinear effect (Geyer and Signell, 1990; Hu et al., 2010a). Further comparisons of the harmonic constants of other tidal components (O_1, K_1, and S_2) at the gauge stations in the TWS and its adjacent sea are summarized in Table 2. The corresponding RMSDs in the amplitudes of the four tidal components (O_1, K_1, M_2, and S_2) were 0.031, 0.071, 0.121, and 0.077 m, respectively, and those for the phase were 26, 17, 16, and 27°, respectively. Table 3 compares the tidal current ellipse parameters (K_1 and M_2) at the specified locations. The RMSDs (0.026 and 0.063 m s^{-1}) in the semi-major axes of K_1 and M_2 are comparable to those (0.046 and 0.027 m s^{-1}) calculated by Jan et al. (2001), who focused on a tidal model of the TWS. The RMSDs in the semi-minor axes of the two tidal components were 0.015 and 0.057 m s^{-1}, and the corresponding values were 0.027 and 0.098 m s^{-1} according to Jan et al. (2001). These comparisons of the tidal parameters show that TFOR can obtain reasonable simulations of the major tidal components in the TWS.

4.4. Velocity comparison

Fig. 8 compares the 36-h low-pass-filtered cross- (U) and along-strait (V) velocity components based on the bm-ADCP observations and the TFOR results. The buoy was deployed in the middle of the TWS (Fig. 1b). The mean and standard deviation for the observed vertically averaged U component in Fig. 8a were –0.1 m s^{-1} and 0.06 m s^{-1}, whereas those for the V component in Fig. 8b were 0.004 m s^{-1} and 0.20 m s^{-1}, thereby implying that the dominant change in the velocity occurs in the along-strait direction. The CC for V between the ADCP observations and TFOR was 0.86. Vertical uniformity was found in the V component for both the observations (Fig. 8e) and model (Fig. 8f), where this uniformity was related to the strong wind stress during the winter. During the wind relaxation period, the V component at the surface was the opposite of that at the bottom of the profile. This type of velocity profile was also reported by Zhu et al. (2008a). The bottom northeastward flow is related to the extension of the KBC, while the surface southwestward flow is related to the CCC (Liao et al., 2013). Lin et al. (2005) also explained that the northward flow, which originates from the PHC, could have a significant impact on this type of V profile. Jan et al. (2006) showed that the subsurface Kuroshio water persists at depths between 100 m and 200 m in the PHC. Another important factor that determines this V profile is the pressure gradient from the southern to the northern tips of Taiwan Island. Yang (2007) used the western boundary layer dynamics to demonstrate that the previous pressure gradient is caused by the KBC. In general, the cross-strait component fluctuates slightly with the northeasterly wind in the winter (Jan et al., 2006; Lin et al., 2005).

In addition, the evaluated tidal energy percentages (rate of tidal energy relative to the total kinetic energy) in the ADCP

Table 3
Tidal current harmonic constants for K_1 and M_2, derived from the observations and model results at the 10 ADCP stations. Ma denotes the semi-major axis in 10^{-2} m s^{-1}, Mi is the semi-minor axis in 10^{-2} m s^{-1}, O is the orientation (unit: °), and G is the phase (unit: °). The reference time for the phase is Greenwich Mean Time (GMT). The observational results are shown below the model data.

St.			K_1				M_2			
No.	N.	E.	Ma	Mi	O	G	Ma	Mi	O	G
1	24.98	119.48	8.8	−0.1	42	294	31.0	22.9	1	211
			9.1	0.1	29	305	29.5	6.5	31	264
2	24.83	119.8	7.7	0.1	74	314	23.6	13.5	66	267
			4.7	1.7	38	238	22.1	10.5	37	252
3	24.65	120.13	6.0	−0.2	77	302	14.1	8.1	65	263
			3.1	1.3	31	223	12.7	6.8	32	233
4	24.47	120.47	6.4	−0.5	80	283	10.5	−0.3	84	224
			1.5	0.0	49	213	5.3	1.0	48	224
5	25	120.13	8.8	−0.5	69	299	34.5	6.9	50	225
			11.3	1.0	40	288	31.0	11.0	25	214
6	23.85	119.87	5.7	1.2	144	51	76.5	6.0	128	15
			7.5	3.3	69	338	69.3	6.0	67	348
7	24.48	119.30	4.0	2.4	101	342	32.1	13.2	123	347
			6.9	1.4	61	325	33.4	10.4	79	340
8	26.29	120.71	6.8	−0.4	180	77	48.1	14.9	171	359
			4.8	1.7	30	265	40.3	15.1	2	174
9	22.63	118.95	14.5	−12.1	77	211	29.3	−12.9	168	12
			16.5	−9.7	139	59	44.5	−17.2	98	359
10	22.28	117.30	12.5	−7.6	41	55	28.9	−11.3	15	225
			12.2	−7.3	101	254	25.7	−9.4	80	40

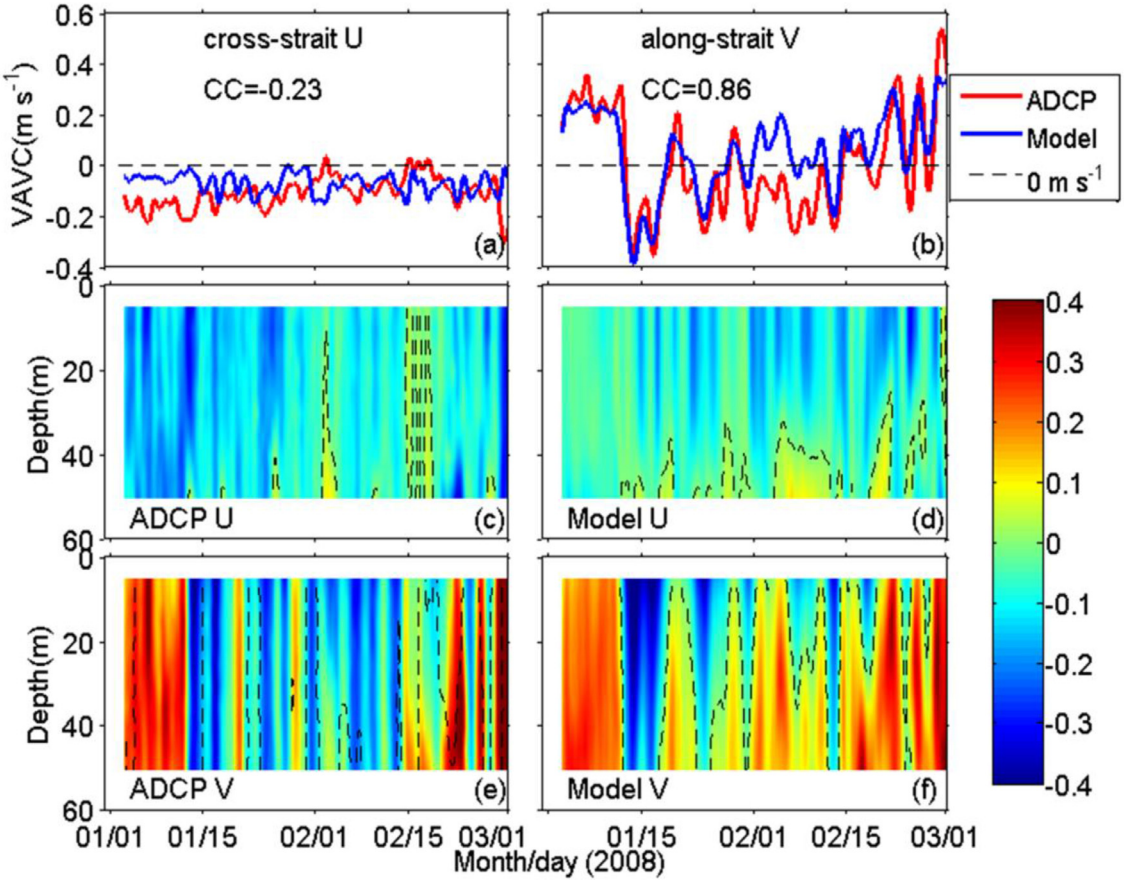

Fig. 8. Comparison of 36-h low-pass-filtered cross-strait (U) and along-strait (V) velocity components obtained from the buoy-mounted ADCP observations and model outputs during January 1 to March 1, 2008 (color bar unit: m s^{-1}). (a–b) Vertically averaged U and V, respectively, with correlation coefficients (CC). (c–f) Time series for U and V obtained from ADCP and model results, where the dotted line indicates the zero contour. The rotating angle of U and V is shown in Fig. 1b. (For interpretation of the references to color in this figure legend, the reader is referred to the web version of this article.)

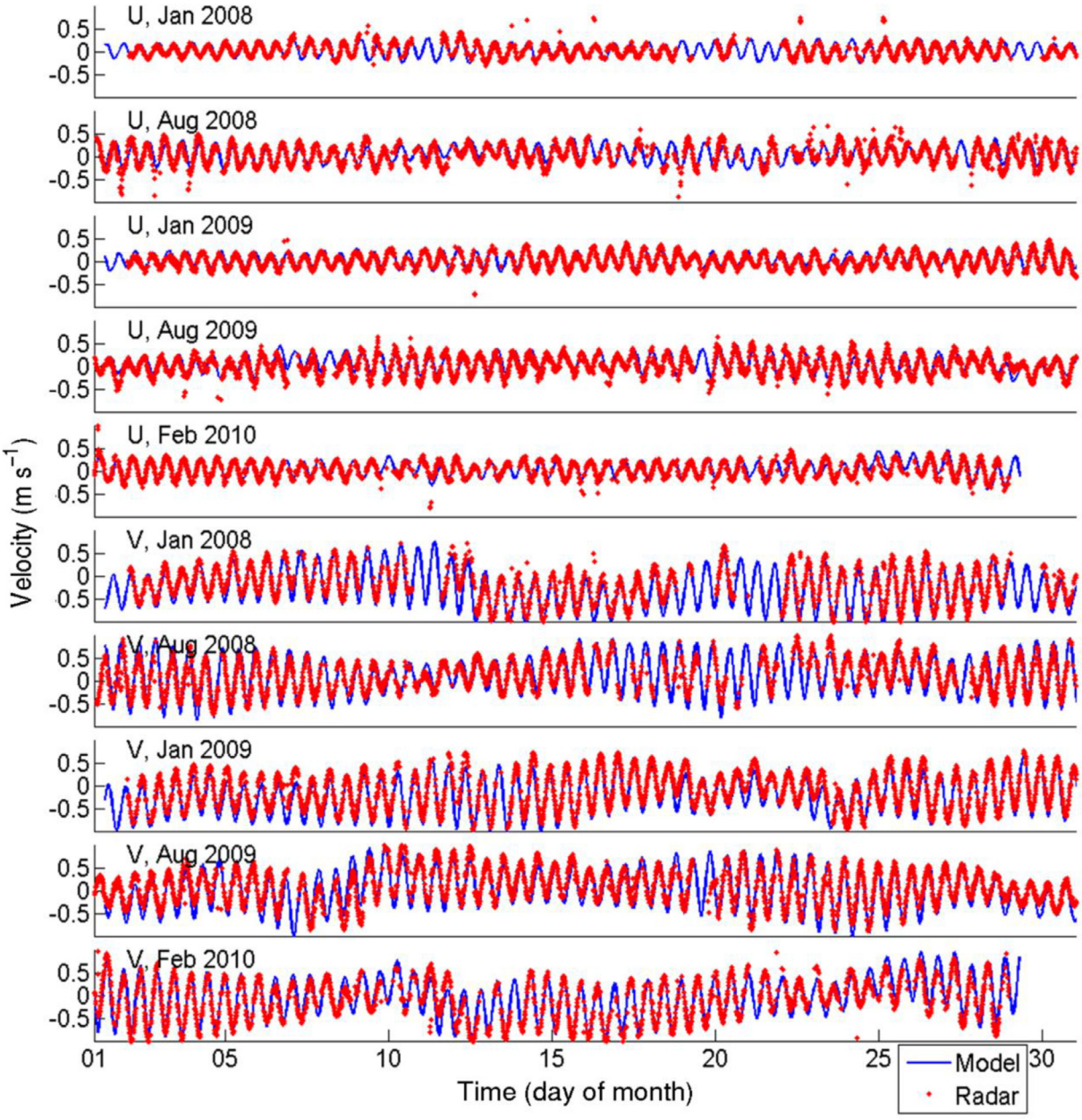

Fig. 9. Comparison of cross-strait (U) and along-strait (V) components of velocity (unit: m s^{-1}) at the radar sample point (indicated by solid triangle in Fig. 1b) in January and August 2008, January and August 2009, and February 2010. The rotating angle of U and V is shown in Fig. 1b.

observations and TFOR results were both higher than 0.8 in the winter and lower than 0.6 in the summer (results not shown). This behavior may be explained by the circulation being weaker in the winter than that in the summer.

Fig. 9 provides a direct comparison of the time series of radar observations and the model simulation at the radar sample point, which was the point for which the most radar samples were available (marked in Fig. 1b). The MB, RMSD, CC, and WS results for the along-strait velocity based on the observations and TFOR results were −0.08 m s^{-1}, 0.19 m s^{-1}, 0.91, and 0.94, respectively, and those for the cross-strait velocity were 0.02 m s^{-1}, 0.12 m s^{-1}, 0.77, and 0.86 (Table 1), thereby indicating that the modeling results were acceptable. It is important to note that the RMSD results were fairly comparable in the cross- and along-strait directions, but the cross-strait velocity range was much less than the along-strait velocity range. The latter result is also indicated in Fig. 7, which shows that the minor-axis (cross-strait) of the ellipse was much smaller than the major-axis at the radar sample point. Moreover, the model performance for the detided components was evaluated by comparing the 36-h low-pass-filtered cross- and along-strait components, as shown in Fig. 10. The MB, RMSD, CC, and WS results were −0.07 m s^{-1}, 0.14 m s^{-1}, 0.73, and 0.87 for the along-strait velocity, respectively, and 0.02 m s^{-1}, 0.06 m s^{-1}, 0.34, and 0.59 for the cross-strait velocity (Table 1). Both the model and the observations showed that the along-strait component was stronger than the cross-strait component and it had a correspondingly larger CC. However, most of the troughs and crests in the along-strait component were reproduced insufficiently well, which may have been related to the use of smoothed forcing data, especially for typhoon processes, such as Kammuri and Sinlaku in August 2008, and Morakot in August 2009. For example, the mean transport during the period August 27 to October 5, 2005 was estimated as 0.35 Sv by Zhang et al. (2009), which is much smaller than the climatological transport estimate for September (2.01 Sv

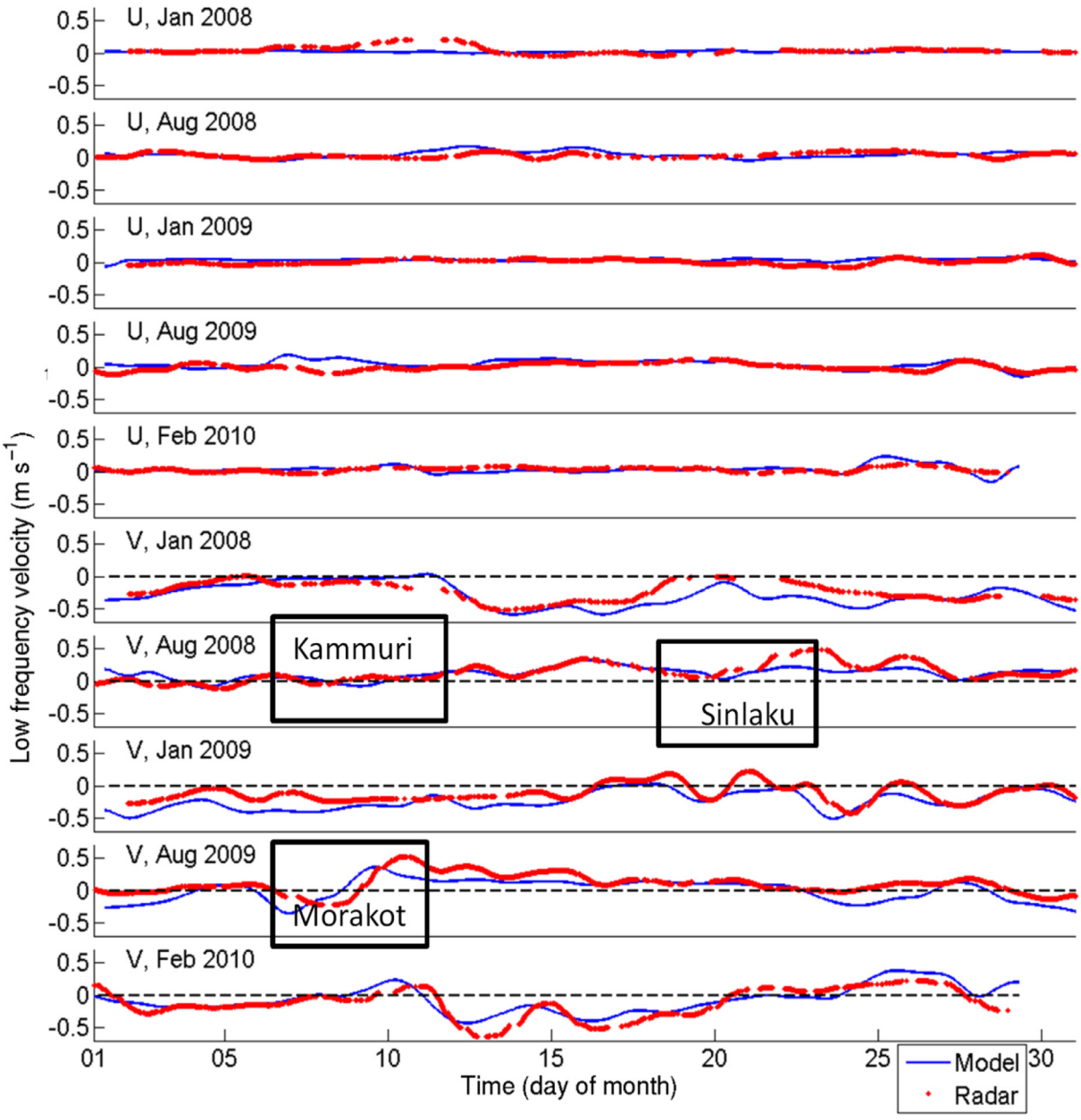

Fig. 10. Comparison of 36-h low-pass-filtered cross-strait (U) and along-strait (V) components of velocity (unit: m s^{-1}) at the radar sample point (indicated by the solid triangle in Fig. 1b). Three periods with typhoons are marked, i.e., Kammuri, Sinlaku, and Morakot. The rotating angle of U and V is shown in Fig. 1b.

northward) given by Chai et al. (2001). The current at the radar sample point flowed northward for almost the entire summer and southward in the winter, although reversals sometimes occurred in the winter. Thus, the southward CCC could reverse northward at the southwestern coast of the TWS during the winter. This phenomenon was reproduced well by the TFOR.

Surface circulation patterns play important roles in maritime search and rescue assistance systems, as discussed subsequently in Section 4.6. According to Zhu et al. (2008a), a vector averaging method was used to estimate the seasonal surface circulation from radar data obtained in the winter and summer of 2008 and 2009. Figs 11a and 11c show the summer surface circulation based on radar and TFOR data, and Figs 11b and 11d show the corresponding winter surface circulation. Similar distributions in the flow directions of the radar data and the TFOR were found in both the summer and winter. However, the distributions of the flow speed obtained from TFOR were much larger than those determined from the radar data. The flow speed rates shown in Fig. 11a range from 0.1 m s^{-1} to 0.2 m s^{-1}, whereas the flow speed in Fig. 11b is approximately 0.1 m s^{-1}. The radar flow speed shown in Fig. 11 is consistent with the monthly circulation data reported by Zhu et al. (2008a).

The CC values between the hourly along-strait wind stress and surface currents obtained from buoys (Fig. 1b) were 0.72 in the summer (June and July, 2013) and 0.69 in the winter (November and December, 2013), and those obtained for TFOR were 0.64 and 0.55, respectively. Both the observations and model had higher correlations in the summer than the winter, thereby indicating that the circulation in the TWS was dominated more by the wind in the summer. The results of the statistical analyses of the winter radar and TFOR data, i.e., MB, RMSD, CC, and WS, were –0.001 m s^{-1}, 0.03 m s^{-1}, 0.77, and 0.76 for the cross-strait component, respectively, and –0.06 m s^{-1}, 0.08 m s^{-1}, 0.76, and 0.58 for the along-strait component. The values of the performance metrics

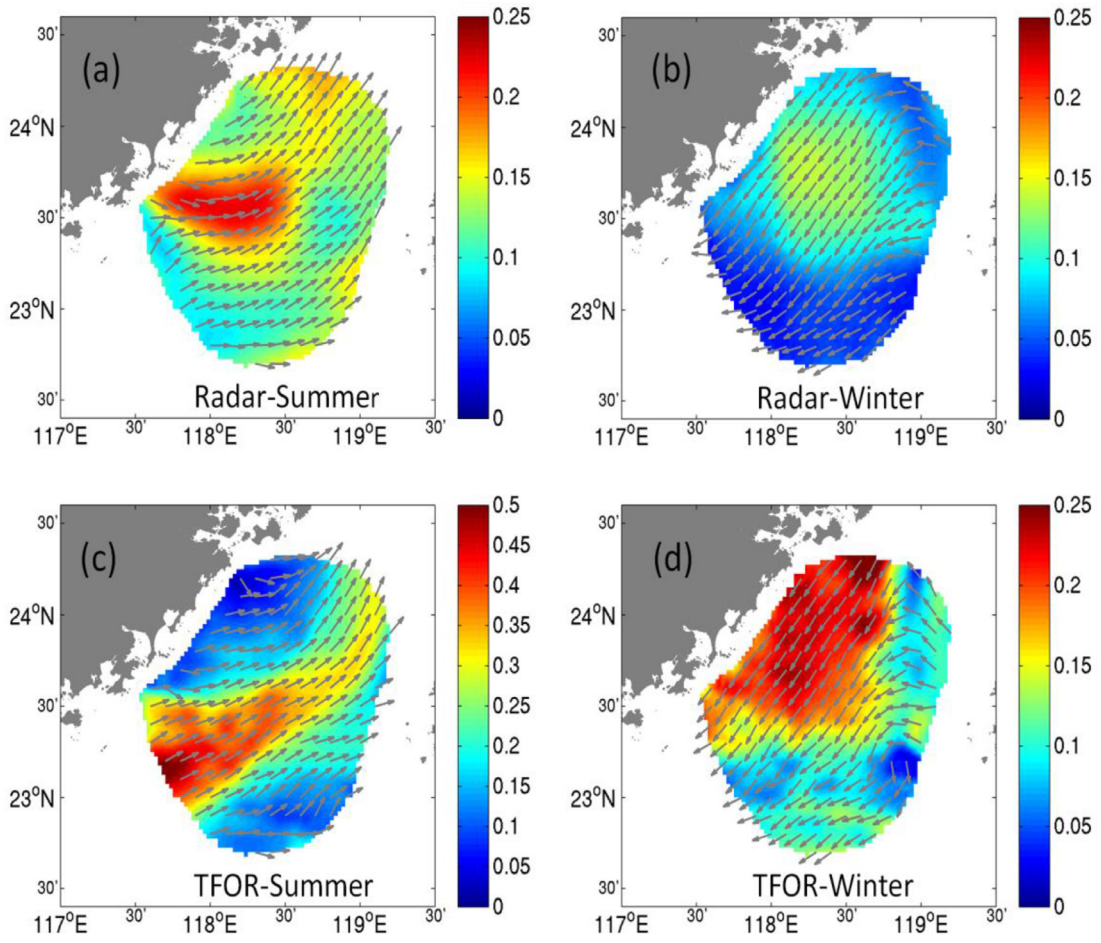

Fig. 11. Seasonal circulation patterns deduced from radar data (a and b) and TFOR (c and d) during the summer (a and c) and winter (b and d). Winter refers to January and February during 2008–2010, and summer refers to August 2008 and July–August 2009. Arrowheads point in the flow directions and color shading represents the flow speed (units: m s^{-1}). (For interpretation of the references to color in this figure legend, the reader is referred to the web version of this article.)

were worse in the summer (Table 1), which may have been related to stronger stratification in the summer when weaker winds prevail. In our previous simulation studies (Jiang et al., 2011; Chen et al., 2014; Liao et al., 2013; Lu et al., 2015; Wang et al., 2013), we found that the flows were easy to simulate in well-mixed regions, whereas those in a stratified region were more difficult to simulate accurately, especially their variance in the vertical direction.

The outputs of the model help us to understand the circulation pattern in the TWS. Fig. 12 shows the mean surface and bottom circulations in the summer (June, July, and August in 2008–2010) and winter (January, February, and December in 2008–2010) estimated from the TFOR results. Fig. 12a shows the Guangdong Coastal Current (GCC, marked in Fig. 1a) at 0.5 m s^{-1} and the extension of the SCS Warm Current in the summer, while Fig. 12b shows the ZCC at 0.4 m s^{-1} in the winter. Hu et al. (2010b) noted that the ZCC flows southwestward with a width of approximately 40 km at approximately 0.45 m s^{-1}. Figs 12c and 12d show a similar flow along the PHC known as the KBC. Jan et al. (2006) demonstrated that in the subsurface layer of the PHC, the Kuroshio water persist throughout the year at depths between 100 m and 200 m.

In summary, TFOR can reproduce the major circulations in the TWS. Two major reasons explain the differences in the circulations based on the radar and TFOR data: errors induced due to the use of the vector averaging method with insufficient radar data and false wind forcing leading to differences in the TFOR circulation. Other potentially sensitive factors include the smoothed bottom topography, monthly mean river discharge, and the model resolution employed in the present study.

4.5. Volume transport

Fig. 13 shows the 30-day moving-average plot of wind stress (https://www.ncdc.noaa.gov/data-access/marineocean-data/blended-global/blended-sea-winds) in the TWS (positive, northeastward; negative, southwestward) and the volume transport through four sections: northern N1–N2, middle M1–M2, southwestern W1–W2, and southeastern E1–E2 (shown in Fig. 1a). The along-strait component of the averaged wind stress over the TWS (Fig. 13a) showed that the northeasterly wind (approximately 0.25 Pa) was dominant in the TWS throughout almost the entire year, except for July and August, when the winds were shifted by the weak southwesterly monsoon (approximately 0.1 Pa). However, the transport through the TWS was positive and northward for almost all of the year (Yang, 2007). The negative, southward transport occurred in the winter, where it usually started at the end of October and continued through January (Fig. 13b). The CC between the transport and wind stress was as high as 0.77, thereby indicating that the monsoon winds have an important effect on the variance in transport through the TWS (Ko et al., 2003; Wu and Hsin, 2005). The statistical analyses showed that the annual (January 1, 2008 to December 31, 2010), spring (March, April, and May in 2008–2010), summer (June, July, and August in 2008–2010), autumn (September, October, and November in 2008–2010), and winter (January, February, and December in 2008–2010) mean transport volumes were 1.16, 1.28, 2.52, 0.80, and 0.04 Sv, respectively, which are consistent with the descriptions given by Jan et al. (2006). Fig. 13c shows the volume transport through the other

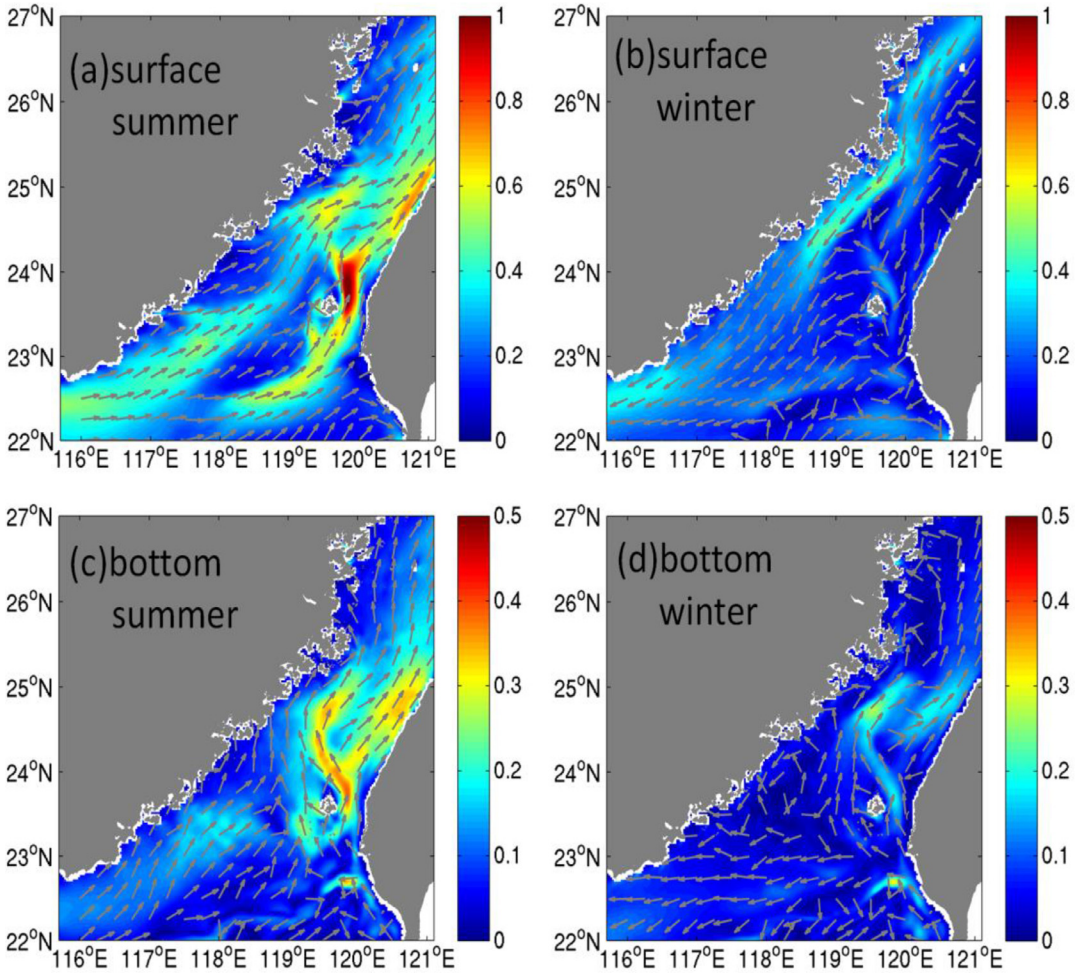

Fig. 12. Seasonal circulation patterns of the top and bottom sigma layer obtained from TFOR simulations. Winter refers to January, February, and December in 2008–2010 and summer refers to June, July, and August in 2008–2010. Arrowheads point in the flow directions and color shading represents the flow speed (units: m s^{-1}). (For interpretation of the references to color in this figure legend, the reader is referred to the web version of this article.)

three sections, i.e., the northern section N1–N2, the southwestern section W1–W2, and the southeastern section E1–E2 (Fig. 1a). The transport through N1–N2 represents the flux in the ZCC (ZM transport) during the winter, through W1–W2 for the Guangdong Coastal Current (GD transport) in summer, and through E1–E2 for the intruding KBC (PH transport). Clearly, these transport volumes had similar variable trends to the TWS transport but they were quite different in amplitude. The year-round northward PH transport peaked at 2.0 Sv in the summer and reached a minimum of 0–0.5 Sv in the winter, whereas the GD transport exhibited comparable reversal transport, i.e., northward at approximately 0.7 Sv in the summer and southward at approximately 0.2–0.5 Sv in the winter. This indicates that the southward ZCC dominates the southern TWS in winter, whereas the Guangdong Coastal Current occupies the region in the summer. Hong et al. (2011b) considered the flow transports through W1–W2 and E1–E2, where the water flows into the TWS in the summer. The transport volume through E1–E2 (PH transport) was approximately 4–10 times the transport through W1–W2 (GD transport). The ZM and GD transport volumes covered the shallow coastal region less than 60 km offshore, which is shallower than 60 m in depth. The ZM transport usually flowed southward, except for weak short-term northward currents that appeared temporarily in the summer. The strongest southward transport occurred in the winter, which was attributable to the ZCC.

The transport through W1–W2 had a bidirectional pattern in the vertical dimension (Hong et al., 2009), and thus the GD transport was divided into two parts by the thermocline at a depth of 25 m. The transport volumes through the upper (red) and bottom (black) layers of W1–W2 are shown in Fig. 13d. Comparable seasonal reversals appeared in the upper and bottom layers. The southward flow was limited almost entirely to the upper layer from October until the next February, and bidirectional currents occurred during the transition from spring to summer as well as from autumn to winter, where the warmer, saltier water flowed northward into the TWS in the bottom layer, whereas the cooler and fresher water in the ZCC flowed southward into the SCS in the surface layer (Zhu et al., 2008a).

4.6. Model application

Based on the available surface currents and winds, a form of Lagrangian tracking algorithm was employed to estimate the possible tracks of floats in the ocean (Jiang et al., 2007; Weng et al., 2009; Oey et al., 2014). According to the track prediction, it was possible to reduce the search scope to save costs and time as well as human lives in shipwrecks. Successful cases include the tracks for the sand barge "JIASEN 6" in October 2009, the fishing boat "XINCHUNMAN 11" in November 2010, and the cargo ship "HUNG CUONG 168" in December 2010. Two cases are shown in Fig. 14, which comprise a long-term lost buoy that was initially deployed in the mid-southern TWS and a short-term search for human lives from a shipwreck. The buoy was unhooked on January 22, 2008

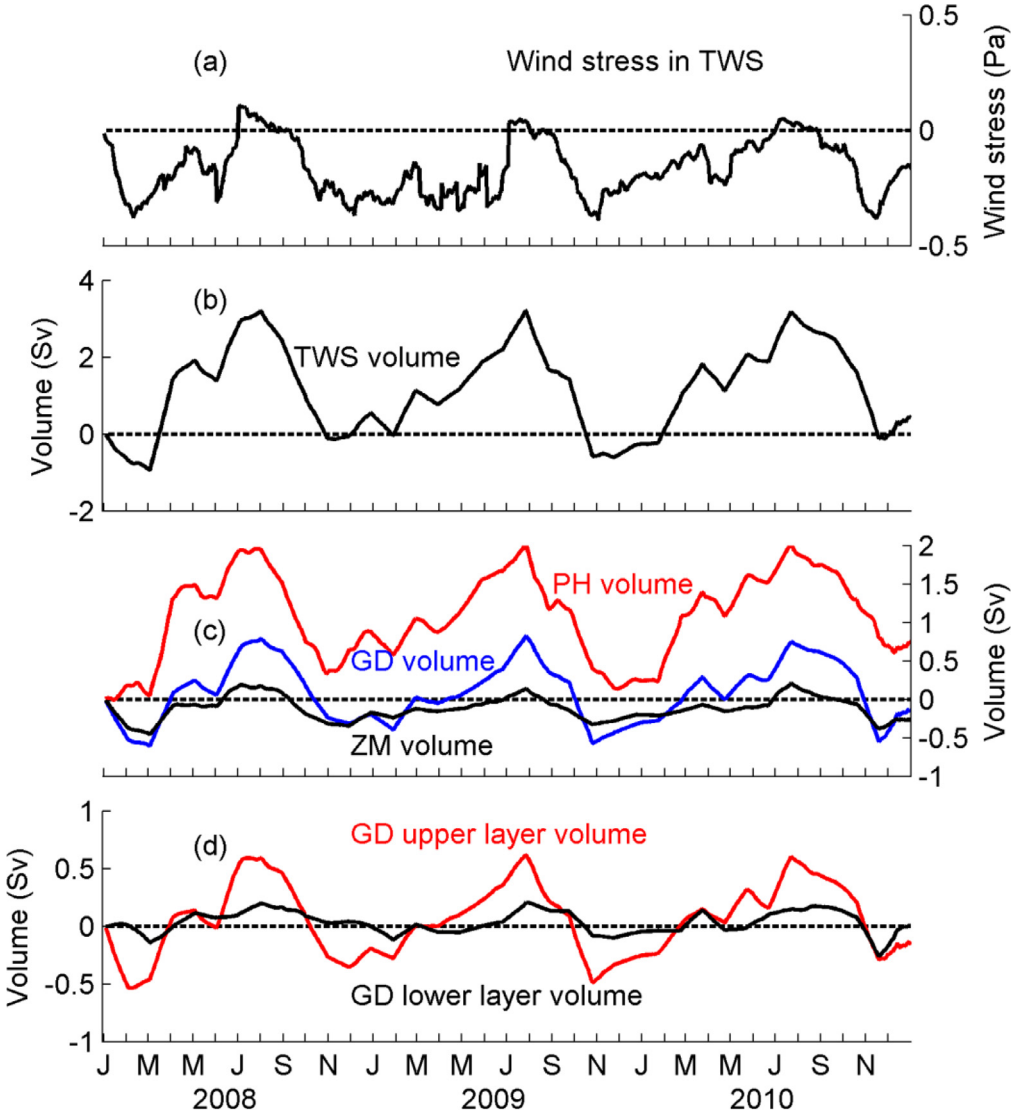

Fig. 13. Time series of 30-day running-mean wind stress (positive, northeastward; negative, southwestward) and volume transport in the Taiwan Strait. The daily 0.25° wind stress (https://www.ncdc.noaa.gov/data-access/marineocean-data/blended-global/blended-sea-winds) in the TWS (Fig. 1a) was used. TWS, GD, PH, and ZM volumes were estimated based on the transport through sections M1–M2, W1–W2, E1–E2, and N1–N2 in Fig. 1b.

(P_1 in Fig. 14a) and it was then located off the northeast tip of Hainan Island by the Global System for Mobile Communications signal from itself on February 5, 2008 (P_2 in Fig. 14a). It was finally found on the southern coast of Vietnam on May 29, 2008 (P_3 in Fig. 14a). Fig. 14a shows that the buoy probably moved along the Hainan and Vietnamese coasts, thereby indicating that the simulated circulation pattern was acceptable within the bounds of the model domain.

Fig. 14b shows the short-term predicted tracks of lost persons during the shipwreck of the cargo ship "HUNG CUONG 168" on December 24, 2010, where the black solid circles indicate the predicted locations of the bodies and the red points indicate where the bodies were found. Based on the predicted trajectories, five people were found 1-h later at M_1 and another eight were found 2-h later at M_2. One remaining person was found near M_3 at 40-h after the shipwreck. However, there were also some failed cases. Shipwrecks often occur during typhoons and the paths of lost people are determined mainly by the sea current and wind speed. However, the impact of waves is sometimes very important, e.g., the Stokes drift related to a wave, which is not considered in the TFOR. In addition, the direct influence of the wind on floaters in the ocean is only evaluated by a simple linear relation, which may introduce some differences compared with the real paths. Information obtained from Fujian Marine Forecasts shows that 198 people have been saved in 343 lost person missions since October, 2009, whereas 98 were never found and 47 were found dead. Overall, 48 predicted tracks have been produced. These applications demonstrate that the outputs of the operational system have acceptable accuracy and they have played an important role in the Fujian Coastal Monitoring System Project.

5. Summary and conclusions

In this study, we described the set up of the TFOR and assessments of its overall performance. The operational TFOR is maintained to provide daily 3-D products in terms of temperature, salinity, and velocity, thereby giving insights into the ocean state in the TWS as well as supporting the maritime search and rescue assistance system (http://www.fjmf.gov.cn/NumPrediction/NumericalPrediction.aspx, 2015). In addition, four-dimensional (4-D) variational data assimilation tests were performed and discussed by Zhang (2009). Radar data assimilation is the most

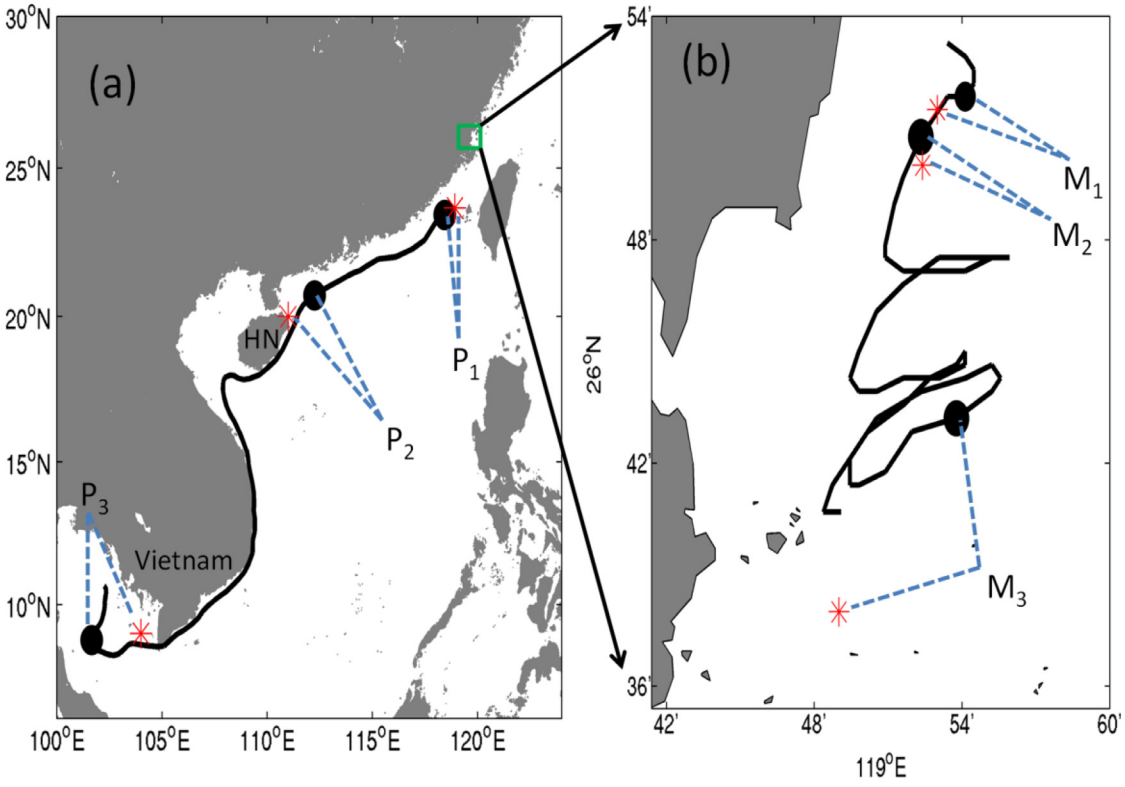

Fig. 14. Track simulations of the lost buoy deployed in the southern TWS (a) and lost people after the "HUNG CUONG 168" shipwreck (b). (a) HN denotes Hainan Island and the green box denotes the shipwreck location, which is enlarged in (b). P_1, P_2, and P_3 indicate the buoy positions on January 22, 2008; February 5, 2008; and May 29, 2008. (b) M_1, M_2, and M_3 denote the three locations at 1-h, 2-h, and 40-h after the shipwreck occurred. The black points denote simulated positions and the red symbols denote real positions. The shipwreck was located at the starting point of the black line near M_1 in (b). The blue dashed lines denote the pairs of real locations and simulated locations.

effective among these tests. At the assimilation stage, the error in radar data assimilation ranges from 0.14 m s^{-1} to 0.17 m s^{-1}, while it ranges from 0.17 m s^{-1} to 0.20 m s^{-1} at the prediction stage. The error in the prediction stage increases rapidly after the first 48-h. The assimilation tests help to improve the performance of the TFOR, but they require too much time (about 10 times longer than that without assimilation). Thus, we do not implement data assimilation in our 10-node cluster system at present, but it will be considered with a higher performance computer system.

Our model–data comparisons based on tracers, temperature, and salinity demonstrated that the model can reproduce the 3-D structure of the hydrographic properties and identify important oceanic processes, such as upwelling and river plumes. Thus, it is reasonable and valuable to use the TFOR results as a reference when planning oceanographic research cruises in the TWS. Comparisons of the SST patterns between the MODIS data and the model results indicated that the intrusion of cold Chinese coastal water into the eastern TWS during the winter changes the SST dramatically and that this change is difficult to replicate, especially in the northwestern part of PHI, where it connects with the KBC and CCC. Nevertheless, the TFOR can reproduce the variations in the SST to an adequate extent and it is useful for further investigation (e.g., Liao et al., 2013). The analyses of the tidal characteristics showed that the distributions of the M_2 tide constants were consistent with previous studies, although the ellipse currents deduced by the model differed slightly from those based on the buoy data. The low frequency currents between the buoy data and model results were comparable and strongly correlated. However, there was a clear difference when gale-strength winds occurred, such as the typhoon processes shown in Fig. 10. Comparisons with radar observations demonstrated that the TFOR simulations were acceptable when sufficient radar observational samples were available. Statistical analyses of the model simulations showed that the mean annual and seasonal transports were comparable to those reported in previous studies. Finally, successful applications to maritime search and rescue operations indicated the reliability and usefulness of the TFOR products.

More efforts will be made to improve the TFOR in future. In particular, a two-way nested model may be considered to obtain a higher horizontal resolution in the TWS, e.g., 1 km. Collecting more accurate bathymetry data will also help to improve the tide simulations. Observational SST should be assimilated in the TFOR to enhance simulations of the temperature and salinity distributions in the TWS. Observational winds in the TWS should be assimilated in the WRF to improve the simulation of subtidal currents in the TWS. Therefore, a higher performance computer system will be employed to implement 4-D variational data assimilation.

Acknowledgments

This study was supported by grants 2013CB955704 from the National Basic Research Program of China (973 Program) Grant no. 2013CB955704, and by grants U1305231 and 41476005 from the Natural Science Foundation of China. We thank three anonymous reviewers and Dr. Federico Ienna for their comments and suggestions on the manuscript.

References

Cai, S.Q., Wang, W.Z., 1997. A numerical study on the circulation mechanism in the northeastern South China Sea and Taiwan Strait. Tropic. Oceanology 16 (1), 7–15 (in Chinese with English abstract).

Chai, F., Xue, H., Shi, M., 2001. The study of horizontal transport in the Taiwan Strait. Oceanogr. China 13, 168–177 (in Chinese with English abstract).
Chang, Y., Lee, K.T., Lee, M.A., Lan, K.W., 2009. Satellite observation on the exceptional intrusion of cold water in the Taiwan Strait. Terr. Atmos. Ocean. Sci. 20, 661–669.
Chapman, D.C., 1985. Numerical treatment of cross-shelf open boundaries in a barotropic coastal ocean model. J. Phys. Oceanogr. 15, 1060–1075.
Chen, C.T.A., 2004. Strait Watch on the Environment and Ecosystem with Telemetry (SWEET). In 2004 Workshop for Oceanographic Research Programs.
Chen, F., 1994. Bays in China. Ocean Press, Beijing, China.
Chen, H., Hu, J.Y., Pan, W.R., Zeng, G.N., Chen, Z.Z., He, Z.G., Zhang, C.Y., Li, H., 2002. Underway measurement of Sea Surface Temperature and Salinity in the Taiwan Strait in August, 1999. Marine Science Bulletin 4, pp. 11–18.
Chen, Z.Y., Yan, X.H., Jiang, Y.W., 2014. Coastal cape and canyon effects on wind–driven upwelling in northern Taiwan Strait. J. Geophys. Res. Oceans 119 (7), 4605–4625.
Chuang, W.S., 1985. Dynamics of subtidal flow in the Taiwan Strait. J. Oceanogr. Soc. Japan 41, 83–90.
Egbert, G.D., Erofeeva, S.Y., 2002. Efficient inverse modeling of barotropic ocean tides. J. Atmos. Oceanic Technol. 19 (2), 183–204.
Flather, R.A., 1976. A tidal model of the northwest European continental shelf. Memo. Soc. Roy. Sci. Liege 6 (10), 141–164.
Fu, Z.L., Hu, J.Y., Yu, G.M., 1991. Seawater flux through Taiwan Strait. Chin. J. Oceanol. Limnol. 9 (3), 232–239.
Gan, J.P., Wang, J.J., Liang, L.L., Li, L., Guo, X.G., 2015. A modeling study of the formation, maintenance, and relaxation of upwelling circulation on the Northeastern South China Sea shelf. Deep Sea Res., Part II 117, 41–52.
Geyer, W.R., Signell, R., 1990. Measurements of tidal flow around a headland with a shipboard acoustic Doppler current profiler. J. Geophys. Res. Oceans 95, 3189–3197.
Guan, B.X., 1978a. The warm current in the South China Sea – a current flowing against the wind in winter in the open sea off Guangdong Province. Oceanol. Limnol. Sinica 9 (2), 117–127 (in Chinese with English abstract).
Guan, B.X., 1978b. New evidences for the South China Sea Warm Current. Mar. Sci. (Suppl.), 100–103 (in Chinese).
Guan, B.X., Chen, S.J., The Current Systems in the Near-Sea Area of China Seas. Technical Report, Institute of Oceanology, Chinese Academy of Sciences, Qingdao, China, 1964, 1–85 (in Chinese with English abstract).
Hong, H.S., Chai, F., Zhang, C.Y., Huang, B.Q., Jiang, Y.W., Hu, J.Y., 2011a. An overview of physical and biogeochemical processes and ecosystem dynamics in the Taiwan Strait. Cont. Shelf Res. 31, S3–S12.
Hong, H.S., Chen, C.T.A., Jiang, Y.W., Lou, J.Y., Chen, Z.Z., Zhu, J., 2011b. Source water of two-pronged northward flow in the southern Taiwan Strait in summer. J. Oceanogr. 67, 385–393.
Hong, H.S., Zheng, Q.A., Hu, J.Y., Chen, Z.Z., Li, C.Y., Jiang, Y.W., Wan, Z.W., 2009. Three-dimensional structure of a low salinity tongue in the southern Taiwan Strait observed in summer. Acta Oceanol. Sin. 28 (4), 1–7.
Hu, C.K., Chiu, C.T., Chen, S.H., Jan, S., Tseng, Y.H., 2010a. Numerical simulation of barotropic tides around Taiwan. Terr. Atmos. 21 (1), 71–84.
Hu, J.Y., Kawamura, H., Hong, H.S., Pan, W.R., 2003. A review of research on upwelling in the Taiwan Strait. Bull. Mar. Sci. 73 (3), 605–628.
Hu, J.Y., Kawamura, H., Li, C.Y., Hong, H.S., Jiang, Y.W., 2010b. Review on current and seawater volume transport through the Taiwan Strait. J. Oceanogr. 66 (5), 591–610.
Jan, S., Chao, S., 2003. Seasonal variation of volume transport in the major inflow region of the Taiwan Strait: the Penghu Channel. Deep Sea Res. Part II 50, 1117–1126.
Jan, S., Chern, C.S., Wang, J., 1994a. Influences of sea surface wind stresses on summertime flow pattern in the Taiwan Strait. Acta Oceanogr. Taiwan. 33, 63–80 (in Chinese).
Jan, S., Chern, C.S., Wang, J., 1994b. A numerical study on currents in the Taiwan Strait during summertime. La Mer 32, 225–234.
Jan, S., Chern, C.S., Wang, J., 1998. A numerical study of current in the Taiwan Strait during winter. Terr. Atmos. Ocean. Sci. 9 (4), 615–632.
Jan, S., Wang, Y.H., Chao, S.Y., Wang, D.P., 2001. Development of a nowcast system for the Taiwan Strait. Ocean Polar Res. 22 (2), 195–203.
Jan, S., Wang, J., Chern, C.S., Chao, S.Y., 2002. Seasonal variation of the circulation in the Taiwan Strait. J. Mar. Syst. 35 (3–4), 249–268.
Jan, S., 2004. The anomalous amplification of M_2 tide in the Taiwan Strait. Geophys. Res. Lett. 31, L07308. doi:10.1029/2003GL019373.
Jan, S., Sheu, D.D., Kuo, H.M., 2006. Water mass and throughflow transport variability in the Taiwan Strait. J. Geophys. Res. 111, C12012. doi:10.1029/2006JC003656.
Jiang, Y.W., Zhang, X., Hong, H.S., Chi, T.H., 2007. Ocean observing data web service and application in shipwreck salvation of Taiwan Strait. In: Zhang, L.J., Watson, T.J., Birman, K.P., Zhang, J. (Eds.), 2007. IEEE International Conference on Web Services Proceedings of IEEE Computer Society. Los Alamitos, pp. 1216–1217.
Jiang, Y.W., Chai, F., Wan, Z.W., Zhang, X., Hong, H.S., 2011. Characteristics and mechanisms of the upwelling in the southern Taiwan Strait: a three-dimensional numerical model study. J. Oceanogr. 67 (6). doi:10.1007/s10872-011-0080-x.
Kara, A.B., Metzger, E.J., Hurlburt, H.E., Wallcraft, A.J., Chassigner, E.P., 2008. Multistatistics metric evaluation of ocean general circulation model sea surface temperature: application to 0.08 Pacific Hybrid Coordinate Ocean Model simulations. J. Geophys. Res. 113 (C12).
Ke, X.H., Hu, J.Y., et al., 1991. Wind field in the central and southern Taiwan Strait. In: Hong, H.S., et al. (Eds.), Minnan-Taiwan Bank Fishing Ground Upwelling Ecosystem Study. Science Press, Beijing, China, pp. 113–120. (in Chinese with English abstract).
Killworth, P.D., Smeed, D.A., Nurser, A.J.G., 2000. The effects on ocean models of relaxation toward observations at the surface. J. Phys. Oceanogr. 30, 160–174.
Ko, D.S., Preller, R.H., Jacobs, G.A., Tang, T.Y., Lin, S.F., 2003. Transport reversals at Taiwan Strait during October and November 1999. J. Geophys. Res. 108 (C11), 3370. doi:10.1029/2003JC001836.
Large, W.G., McWilliams, J.C., Doney, S.C., 1994. Oceanic vertical mixing: a review and a model with a nonlocal boundary layer parameterization. Rev. Geophys. 32, 363–403.
Liang, W.D., Tang, T.Y., Yang, Y.J., Ko, M.T., Chuang, W.S., 2003. Upper-ocean currents around Taiwan. Deep Sea Res., Part II 50 (6–7), 1085–1105. doi:10.1016/S0967-0645(03)00011-0.
Liao, E.H., Jiang, Y.W., Li, L., Hong, H.S., Yan, X.H., 2013. The cause of the 2008 cold disaster in the Taiwan Strait. Ocean Model. 62, 1–10.
Lin, S.F., Tang, T.Y., Jan, S., Chen, C.J., 2005. Taiwan Strait current in winter. Cont. Shelf Res. 25, 1023–1042. doi:10.1016/j.csr.2004.12.008.
Liu, Y.G., Parker, M.C., Barbara, M.H., Edward, P.D., Kosro, P.M., Neil, S.B., 2009. Evaluation of a coastal ocean circulation model for the Columbia River plume in summer 2004. J. Geophys. Res. 114, C00B04. doi:10.1029/2008JC004929.
Lu, W., Yan, X.H., Jiang, Y., 2015. Winter bloom and associated upwelling northwest of the Luzon Island: a coupled physical-biological modeling approach. J. Geophys. Res. Oceans 120, 533–546. doi:10.1002/2014JC010218.
Mellor, G.L., Oey, L.Y., Ezer, T., 1998. Sigma coordinate pressure gradient errors and the Seamount problem. J. Atmos. Ocean. Technol. 15, 1122–1131.
Nitani, H., 1972. Beginning of the Kuroshio. In: Stommel, H., Yoshida, K. (Eds.), Kuroshio: Its Physical Aspects. University of Tokyo Press, Tokyo, pp. 129–163.
Oey, L.Y., Chang, Y.L., Lin, Y.C., Chang, M.C., Xu, F., Lu, H.F., 2013. ATOP-the advanced Taiwan ocean prediction system based on the mpiPOM. Part 1: model descriptions, analyses and results. Terr. Atmos. Ocean. Sci. 24 (1).
Oey, L.Y., Chang, Y.L., Lin, Y.C., Chang, M.C., Varlamov, S., Miyazawa, Y., 2014. Cross flows in the Taiwan Strait in winter. J. Phys. Oceanogr. 44 (3), 801–817.
Pawlowicz, R., Beardsley, B., Lentz, S., 2002. Classical tidal harmonic analysis with errors in Matlab using t-tide. Comput. Geosci. 28, 929–937.
Shchepetkin, A.F., McWilliams, J.C., 2003. A method for computing horizontal pressure-gradient force in an oceanic model with a nonaligned vertical coordinate. J. Geophys. Res. Oceans 108 (C3), 3090. doi:10.1029/2001JC001047.
Shchepetkin, A.F., McWilliams, J.C., 2005. The regional oceanic modeling system (ROMS): a split-explicit, free-surface, topography-following-coordinate oceanic model. Ocean Model. 9, 347–404.
Song, Y., Haidvogel, D.B., 1994. A semi-implicit ocean circulation model using a generalized topography-following coordinate system. J. Comp. Phys. 115 (1), 228–244.
Wang, J., Hong, H.S., Jiang, Y.W., Chai, F., Yan, X.H., 2013. Summer nitrogenous nutrient transport and its fate in the Taiwan Strait: a coupled physical-biological modeling approach. J. Geophys. Res. Oceans 118, 4184–4200.
Wang, Y.H., Jan, S., Wang, D.P., 2003. Transports and tidal current estimates in the Taiwan Strait from shipboard ADCP observations (1999–2001). Estuar. Coast. Shelf Sci. 57 (1–2), 193–199.
Weng, Y.C., Yang, J.X., Jiang, Y.W., 2009. Simulation of floater trajectory in Taiwan Strait. J. Xiamen Univ. (Nat. Sci.) 48 (3), 446–449 (in Chinese with English abstract).
Willmott, C.J., 1981. On the validation of models. Phys. Geogr. 2, 184–194.
Wyrtki, K., Physical Oceanography of the Southeast Asia Waters. Scientific Results of Marine Investigations of the South China Sea and Gulf of Thailand, 1959–1961, Naga Report Vol. 2, 195.
Wu, C.R., Hsin, Y.C., 2005. Volume transport through the Taiwan Strait: a numerical study. Terr. Atmos. Ocean. Sci. 16 (2), 377–391.
Wu, C.R., Chao, S.Y., Hsu, C., 2007. Transient, seasonal and interannual variability of the Taiwan Strait current. J. Oceanogr. 63, 821–833.
Yang, J., 2007. An oceanic current against the wind: How does Taiwan Island steer warm water into the East China Sea? J. Phys. Oceanogr. 37, 2563–2569.
Zhang, W.Z., Hong, H.S., Shang, S.P., Yan, X.H., Chai, F., 2009. Strong southward transport events due to typhoons in the Taiwan Strait. J. Geophys. Res. 114 (C11).
Zhang, Z.C., 2009. Studies on Computation of the Three-Dimensional Hydrodynamic Parallel Model Ph.D. Thesis. Xiamen University (in Chinese with English abstract).
Zhu, D.Y., Li, L., Li, Y., Guo, X.G., 2008a. Seasonal variation of surface currents in the southwestern Taiwan Strait observed with HF radar. Chin. Sci. Bull. 53 (15), 2385–2391.
Zhu, D.Y., 2008b. Applications of High Frequency Ground Wave Radar to Coastal Ocean – A Case Study in the Taiwan Strait Ph.D. Thesis. Xiamen University (in Chinese with English abstract).